Nonlinear Shelf Waves in a Rotating Annulus

Andrew Stewart

October 13, 2009

1 Introduction

Shelf breaks are a ubiquitous and dynamically important feature in the topography of the coastal oceans. A region of particular interest is the southeastern coast of Africa, where the Agulhas current flows southwest at speeds of up to 1 ms^{-1} over a shelf break [2]. This has motivated a series of dynamical investigations. Gill and Schumann [6] studied the influence of topography on a coastal jet with specific application to the Agulhas current, whilst Mysak and others have considered the phenomenon of coastally-trapped waves [19, 20, 21].

Where there is a very sharp drop from the coastal shelf to the ocean floor, the topography may be approximated by a discontinuity in depth, an approach that is appealing due to its analytical simplicity. This approach was first used to study coastally-trapped waves by Longuet-Higgins [17], and was subsequently applied to coastal currents by Johnson [10, 13].

The present work concerns a model for nonlinear Rossby shelf waves propagating along a discontinuity in depth that was first developed by Haynes et al [7], who derived a fully nonlinear wave equation that is valid in the limit of infinitely long waves. This model, which will be discussed further in Section 3, was subsequently extended to include higher-order dispersive terms [3, 11]. In the weakly nonlinear limit, the model reduces to a Korteweg-de Vries (KdV)-type equation [4], which will be discussed in Section 4. These models, and the broader subject of Rossby wave hydraulics, were reviewed by Johnson & Clarke [12].

The theory of nonlinear Rossby shelf waves hinges upon the assumption of columnar motion in the fluid, even when it crosses the step, which has motivated several studies [9, 14, 15] of the interaction of vortices with step topography. In a recent experiment [8], dipoles fired over a step were shown largely to maintain their columnar structure, albeit with some additional diffusion of vorticity. This suggests that fluid columns in a shallow rotating flow will be preserved across a discontinuity in depth.

The goal of this project is to generate nonlinear Rossby shelf waves experimentally and compare their properties with theoretical predictions. Whilst the previous theory is based on an infinitely long straight channel, we have constructed our experiment in an annulus, and we will show that analogous theoretical results hold in this geometry. We will first introduce the set-up of the laboratory experiment and reformulate the finite-amplitude and weakly nonlinear wave equations for the annular domain. We will then discuss the inclusion of bottom friction in the model and its effect on the waves, and analyse some instabilities that were found to arise in the course of the experiment. Finally, we will present some experimental results for breaking lee waves and compare them with numerical simulations based on the finite-amplitude wave equation.

2 Experimental Set-Up

The theoretical analysis presented in this report has been motivated by the laboratory experiment that served as the focus of this project. In this section we will only provide an overview of the experiment, postponing a discussion of the results to Sections 6 and 7.

The experiment was designed to replicate the theoretical investigations of [7], who studied the behaviour of waves propagating about a discontinuity in depth in a straight channel with a rigid lid in a rotating frame. The most practical way to achieve this in the laboratory was to create an annular channel in a cylindrical tank on a rotating table. A shelf of width 10.5 cm and height 5.0 cm was built around the outer edge of the tank, which measured approximately 2.13 m in diameter, to create a discontinuity in depth, and a weighted sheet of flexible plastic was used to create the inner wall of the annulus. A photograph of this apparatus is shown in Figure 1.

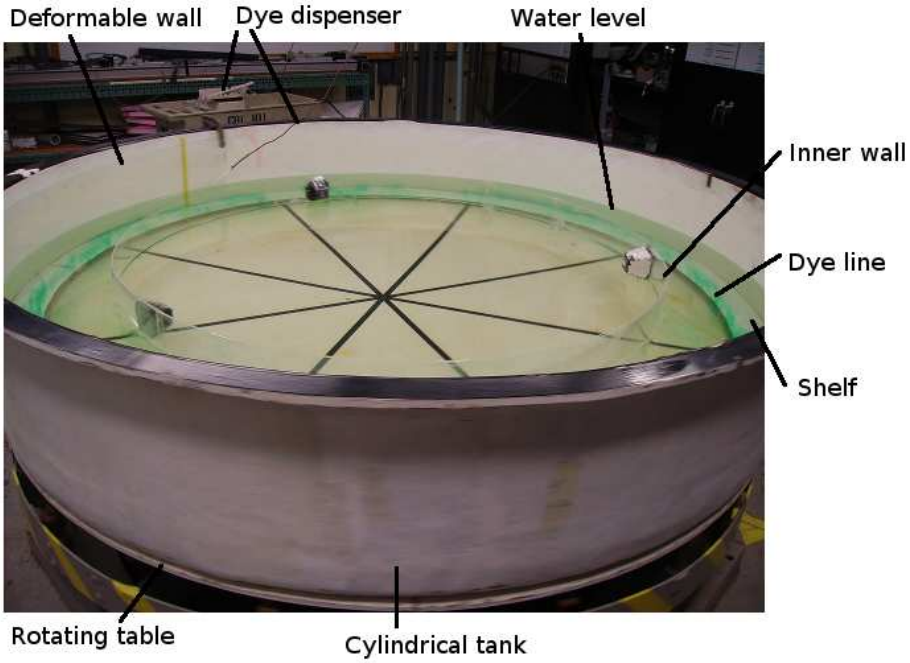

Figure 1: A photograph of the experimental set-up.

To perform the experiments, we filled the tank with water to a prescribed depth, typically 10 – 25 cm above the base of the tank, and then accelerated it to a constant angular velocity. We then left the tank to rotate until the fluid inside had reached a stationary state in the rotating frame of reference. We perturbed the fluid from this state either by the moving a deformable wall attached to the edge of the tank, or by creating a bump in the outer wall and rapidly changing the rate of rotation of the tank. To visualise the flow, we dispensed a line of dye into the fluid directly above the shelf line (along the potential vorticity interface) and recorded the results with a digital camera that positioned directly above the centre of the tank and made to rotate at the same speed as the tank.

This experiment does not perfectly replicate the theoretical conditions of [7], most obviously because the channel is curved rather than straight. We have therefore modified and extended the previous theory accordingly, and this will be covered in the following sections. Note also that the inner wall is not sealed against the bottom of the tank, thereby permitting a small flux of fluid between the outer annulus and the central part of the tank, and that the fluid has a free surface that deforms under the influence of the centrifugal force, rather than a rigid lid. However, both of these effects were found to make negligible contributions to the behaviour of the fluid.

Another theoretical inconsistency arises from the fact that the ratio of the depth of the fluid to the width of the channel is typically close to 1, casting doubt upon the validity of the shallow water theory. In practice the rate of rotation of the tank was sufficiently high as to ensure approximately columnar motion anyway, so the shallow water theory may be expected to hold quite well. In fact, the most important deviation from the theory was the absolute discontinuity in the depth at the shelf line, which in theory is an approximation of a steep slope. In later experiments a slope of width 2.5 cm was added to the end of the shelf, substantially altering the behaviour of the experiment.

3 Topographic Rossby Waves in a Rotating Annulus

We shall now reformulate the theory of [3] for application to the annular domain of the laboratory experiment. The fluid lies in the region $R_w(\theta) \leq r \leq R_c(\theta)$, $0 \leq \theta \leq 2\pi$, $h(r) \leq z \leq H$, where h is the height of the bottom topography,

$$h = \begin{cases} 0, & R_w < r < R_h \\ H_s, & R_h < r < R_c \end{cases}, \tag{1}$$

and $r = R_h(\theta)$ is the equation of the shelf line. Here we have applied the rigid lid approximation, assuming that perturbations to the upper surface of the fluid are much smaller than the average depth H. A diagram of this set-up is presented in Figure 2.

We assume that the flow is sufficiently shallow ($H \ll R_c - R_w$), and has sufficiently small topography ($H_s \ll H$), that it is governed approximately by the shallow water quasigeostrophic equation for fluid under a rigid lid,

$$\frac{\mathrm{D}q}{\mathrm{D}t} = 0, \quad q = \nabla^2\Psi + \frac{fh}{H}, \tag{2}$$

where f is the Coriolis parameter and q is the quasigeostrophic potential vorticity. Here $\Psi = p_s/f\rho$ is the quasigeostrophic streamfunction, where p_s is the pressure at the rigid lid and ρ is the density of the fluid. With this definition, Ψ satisfies

$$u = -\frac{1}{r}\frac{\partial\Psi}{\partial\theta}, \quad v = \frac{\partial\Psi}{\partial r}, \tag{3}$$

and the velocity field is $\mathbf{u} = u\mathbf{e_r} + v\mathbf{e}_\theta$, such that $\omega = (\nabla \times \mathbf{u}) \cdot \hat{\mathbf{z}} = \nabla^2\Psi$.

We prescribe a mean flow $\mathbf{u}_m = -\nabla \times \psi_m(r,\theta)\hat{\mathbf{z}}$ in the channel, modelling the presence of an along-shore current in the real ocean. We require that the flow should be unidirectional,

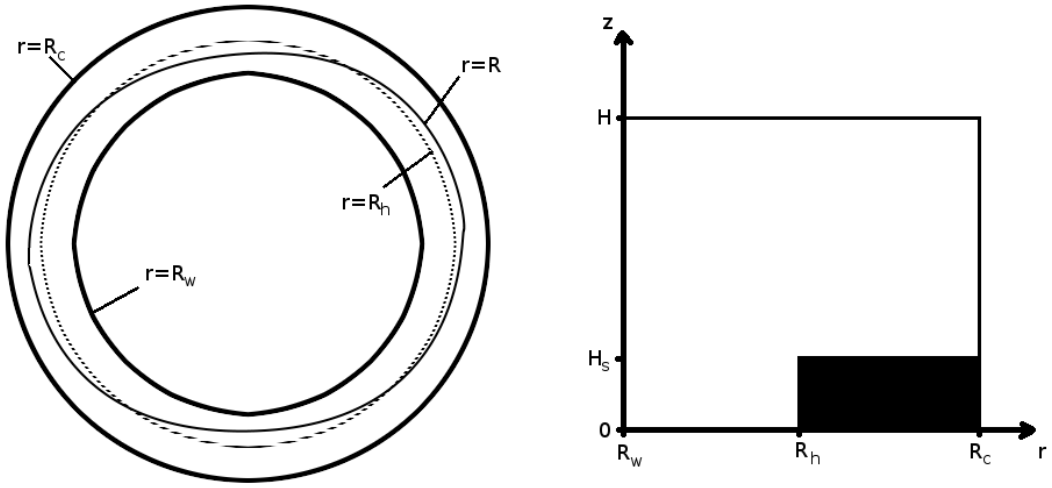

Figure 2: Top-down (left) and side-on (right) views of the physical set-up for the model.

that the walls $r = R_w$ and $r = R_c$ should be streamlines, and that the volume flux should be constant around the annulus,

$$\frac{\partial}{\partial\theta}\int_{R_w(\theta)}^{R_c(\theta)} v_m \mathrm{d}r = 0. \tag{4}$$

Here we neglect the contribution to the volume from the variation of the bottom topography in order to be consistent with the quasigeostrophic approximation. We also require that the vorticity of the mean flow should be materially conserved. These requirements may be met in a radially symmetric annulus, but when R_w and R_c vary with θ we must allow for bidirectional flow to find a steady solution. We must therefore prescribe a mean flow streamfunction that approximately satisfies these conditions,

$$\psi_m = \tfrac{1}{2}\overline{\Omega_m}\frac{\left(\overline{R_c}^2 - \overline{R_w}^2\right)\left(r^2 - R_w^2\right)}{R_c^2 - R_w^2}, \tag{5}$$

where an overbar $\overline{\ }$ denotes the value of a function at some fixed $\theta = \theta_m$. This mean flow satisfies all requirements except that its vorticity should be materially conserved, which is only approximately satisfied under the assumption that the walls of the annulus vary very slowly with θ,

$$\left|\frac{\partial R_w}{\partial\theta}\right|, \left|\frac{\partial R_c}{\partial\theta}\right| \ll 1 \implies \frac{\mathrm{D}\omega}{\mathrm{D}t} \approx 0. \tag{6}$$

In the case that R_w and R_c do not vary with θ, (5) reduces to a flow of constant angular velocity and exactly satisfies the above requirements.

It is now convenient to write the overall streamfunction as

$$\Psi = \psi_m + \psi(r, \theta, t), \tag{7}$$

where the first term corresponds to the mean flow and the second to any deviation. On applying (6), the potential vorticity equation (2) then becomes

$$\frac{\mathrm{D}q'}{\mathrm{D}t} \approx 0, \quad q' = \nabla^2\psi + \frac{fh}{H}, \tag{8}$$

Suppose that the fluid is perturbed from a basic state in which the only motion is that of the mean flow, such that $\nabla^2\psi = 0$ and

$$q' = \begin{cases} 0, & R_w < r < R_h \\ Q, & R_h < r < R_c \end{cases}. \tag{9}$$

We denote the position of the interface between these regions of differing potential vorticity as $r = R(\theta, t)$, assuming that this interface remains single-valued in θ. If in some region $R > R_h$ then, by conservation of potential vorticity, we have

$$\begin{aligned} q' = \nabla^2\psi + 0 = 0 \quad &\implies \nabla^2\psi = 0 \quad && \text{in } R_w < r < R_h, \\ q' = \nabla^2\psi + Q = 0 \quad &\implies \nabla^2\psi = -Q \quad && \text{in } R_h < r < R, \\ q' = \nabla^2\psi + Q = Q \quad &\implies \nabla^2\psi = 0 \quad && \text{in } R < r < R_c, \end{aligned}$$

and if $R < R_h$ then

$$\begin{aligned} q' = \nabla^2\psi + 0 = 0 \quad &\implies \nabla^2\psi = 0 \quad && \text{in } R_w < r < R, \\ q' = \nabla^2\psi + 0 = Q \quad &\implies \nabla^2\psi = Q \quad && \text{in } R < r < R_h, \\ q' = \nabla^2\psi + Q = Q \quad &\implies \nabla^2\psi = 0 \quad && \text{in } R_h < r < R_c, \end{aligned}$$

which may be expressed succinctly as the following Poisson equation for the streamfunction,

$$\nabla^2\psi = Q\left(\mathcal{H}(r - R) - \mathcal{H}(r - R_h)\right), \tag{10}$$

where $\mathcal{H}$ denotes the Heaviside step function. We also require that the streamfunction vanishes on the boundaries of the annulus,

$$\psi = 0 \text{ on } r = R_w \text{ and } r = R_c. \tag{11}$$

Finally, we require that particles on the interface $r = R$ remain on the interface, i.e. $D/Dt(r - R) = 0$, which leads to the following condition,

$$\frac{\partial R}{\partial t} = -\frac{1}{R}\frac{\partial}{\partial\theta}\Psi(R(\theta, t), \theta, t). \tag{12}$$

We now define a length scale $L = \overline{R_c} - \overline{R_w}$ and nondimensionalise $r = L\hat{r}$, $t = Q^{-1}\hat{t}$ and $\psi = QL^2\hat{\psi}$, where a hat $\hat{}$ denotes a dimensionless variable. This yields the following system of dimensionless equations,

$$\frac{\partial^2\hat{\psi}}{\partial\hat{r}^2} + \frac{1}{\hat{r}}\frac{\partial\hat{\psi}}{\partial\hat{r}} + \frac{1}{\hat{r}^2}\frac{\partial^2\hat{\psi}}{\partial\theta^2} = \mathcal{H}\left(\hat{r} - \hat{R}\right) - \mathcal{H}\left(\hat{r} - R_H\right), \tag{13a}$$

$$\hat{\psi} = 0 \text{ on } \hat{r} = R_I \text{ and } \hat{r} = R_O, \tag{13b}$$

$$\frac{\partial\hat{R}}{\partial\hat{t}} = -\frac{1}{\hat{R}}\frac{\partial}{\partial\theta}\hat{\Psi}\left(\hat{R}\left(\theta, \hat{t}\right), \theta, \hat{t}\right), \tag{13c}$$

where $R_H = R_h/L$, $R_I = R_w/L$ and $R_O = R_c/L$ are the dimensionless radii of the annulus. We will henceforth drop the hat notation for dimensionless variables. We seek long wave solutions by prescribing that the width of the channel should be small compared to the circumference of the shelf line and assuming that the solution varies slowly with θ and t,

$$\theta = \mu^{-1/2}\phi, \quad t = \mu^{-1/2}\tau, \tag{14}$$

where $\mu = (L/2\pi\overline{R_h})^2 \ll 1$. Equations (13a)–(13c) then take the form,

$$\frac{\partial^2\psi}{\partial r^2} + \frac{1}{r}\frac{\partial\psi}{\partial r} + \frac{\mu}{r^2}\frac{\partial^2\psi}{\partial\phi^2} = \mathcal{H}(r-R) - \mathcal{H}(r-R_H), \tag{15a}$$

$$\psi = 0 \text{ on } r = R_I \text{ and } r = R_O, \tag{15b}$$

$$\frac{\partial R}{\partial\tau} = -\frac{1}{R}\frac{\partial}{\partial\phi}\Psi(R(\phi,\tau),\phi,\tau). \tag{15c}$$

We now expand ψ asymptotically in the small parameter μ,

$$\psi = \psi^{(0)} + \mu\psi^{(1)} + \mu^2\psi^{(2)} + \dots. \tag{16}$$

Substituting this in to (15a) we find that the leading order equation is

$$\frac{\partial^2\psi^{(0)}}{\partial r^2} + \frac{1}{r}\frac{\partial\psi^{(0)}}{\partial r} = \mathcal{H}(r-R) - \mathcal{H}(r-R_H), \tag{17}$$

which may be solved subject to the boundary conditions (15b) to give

$$\begin{aligned}\psi^{(0)} = {} & \tfrac{1}{4}\left(r^2 - R^2\right)\mathcal{H}(r-R) - \tfrac{1}{4}\left(r^2 - R_H^2\right)\mathcal{H}(r-R_H) \\ & + \tfrac{1}{2}R_H^2\mathcal{H}(r-R_H)\ln(r/R_H) - \tfrac{1}{2}R^2\mathcal{H}(r-R)\ln(r/R) \\ & + \frac{\ln(r/R_I)}{\ln(R_O/R_I)}\left[\tfrac{1}{2}R^2\ln(R_O/R) - \tfrac{1}{2}R_H^2\ln(R_O/R_H) + \tfrac{1}{4}\left(R^2 - R_H^2\right)\right].\end{aligned} \tag{18}$$

We may substitute this leading-order streamfunction in to (15c), but we then obtain a non-dispersive evolution equation for R. This may be remedied by continuing the expansion of (15a) to $\mathrm{O}(\mu)$,

$$\frac{\partial^2\psi^{(1)}}{\partial r^2} + \frac{1}{r}\frac{\partial\psi^{(1)}}{\partial r} + \frac{1}{r^2}\frac{\partial^2\psi^{(0)}}{\partial\phi^2} = 0, \tag{19}$$

which we solve to find the following expression for $\psi^{(1)}$,

$$\begin{aligned}\psi^{(1)} = {} & \tfrac{1}{6}\frac{\partial}{\partial\phi}\left\{RR_\phi\ln^3(r/R)\mathcal{H}(r-R) - R_HR_{H\phi}\ln^3(r/R_H)\mathcal{H}(r-R_H)\right\} \\ & + \frac{\ln(r/R_I)}{\ln(R_O/R_I)}\left\{\tfrac{1}{6}\left(R_HR_{H\phi}\right)_\phi\ln^3(R_O/R_H) - \tfrac{1}{2}R_{H\phi}^2\ln^2(R_O/R_H)\right. \\ & \qquad \left. - \tfrac{1}{6}\left(RR_\phi\right)_\phi\ln^3(R_O/R) + \tfrac{1}{2}R_\phi^2\ln^2(R_O/R)\right\} \\ & + \ln(R_O/r)\ln(r/R_I)\left\{\tfrac{1}{6}\ln(R_Or/R_I^2)\frac{\partial^2}{\partial\phi^2} - \frac{R_{I\phi}}{R_I}\frac{\partial}{\partial\phi} + \frac{R_{I\phi}^2 - R_IR_{I\phi\phi}}{2R_I^2}\right\}G,\end{aligned} \tag{20}$$

where

$$G(\phi,\tau)=\frac{\frac{1}{2}R^2\ln(R_O/R)-\frac{1}{2}R_H^2\ln(R_O/R_H)+\frac{1}{4}(R^2-R_H^2)}{\ln(R_O/R_I)}. \tag{21}$$

Substituting (18) and (20) into (15c) yields the following evolution equation for finite-amplitude waves on the interface,

$$\begin{aligned}\frac{\partial R}{\partial\tau}=-\frac{1}{R}\frac{\partial}{\partial\phi}\Bigg\{&\tfrac{1}{2}\alpha_m\frac{\left(\overline{R_O}^2-\overline{R_I}^2\right)\left(R^2-R_I^2\right)}{R_O^2-R_I^2}\\
&+\ \mathcal{H}(R-R_H)\left[\tfrac{1}{2}R_H^2\ln(R/R_H)+\tfrac{1}{4}(R_H^2-R^2)\right]+\ln(R/R_I)\,G\\
&+\ \mu\Bigg\{\mathcal{H}(R-R_H)\left[\tfrac{1}{2}R_{H\phi}^2\ln^2(R/R_H)-\tfrac{1}{6}\left(R_HR_{H\phi}\right)_\phi\ln^3(R/R_H)\right]\\
&+\ \frac{\ln(R/R_I)}{\ln(R_O/R_I)}\left[\tfrac{1}{6}\left(R_HR_{H\phi}\right)_\phi\ln^3(R_O/R_H)-\tfrac{1}{2}R_{H\phi}^2\ln^2(R_O/R_H)\right.\\
&\qquad\left.-\ \tfrac{1}{6}\left(RR_\phi\right)_\phi\ln^3(R_O/R)+\tfrac{1}{2}R_\phi^2\ln^2(R_O/R)\right]\\
&+\ \ln(R_O/R)\ln(R/R_I)\left[\tfrac{1}{6}\ln(R_OR/R_I^2)\frac{\partial^2}{\partial\phi^2}-\frac{R_{I\phi}}{R_I}\frac{\partial}{\partial\phi}+\frac{R_{I\phi}^2-R_IR_{I\phi\phi}}{2R_I^2}\right]G\Bigg\}\Bigg\},\end{aligned} \tag{22}$$

where $\alpha_m=\overline{\Omega_m}/Q$. We may obtain higher-order approximations to the streamfunction, and thereby to the evolution equation (22), by solving further equations with the same form as (19), but the expressions involved quickly become unmanagable.

It is important to note that whilst we can account for azimuthally varying R_w, R_h and R_c, we are unable to apply this theory in the limits as (a) $R_w\to 0$ or (b) $R_c\to\infty$ uniformly. We can still apply a long-wave scaling in these cases by redefining $L=\overline{R_c}-\overline{R_h}$ or $L=\overline{R_h}-\overline{R_w}$ respectively. In case (a) the asymptotic expansion breaks down when $r=\mathrm{O}\left(\mu^{1/2}\right)$ because the derivative with respect to ϕ in (15a) is then $\mathrm{O}\,(1)$. In case (b) we require that $|\mathbf{u}|\to 0$ as $r\to\infty$ so that the total energy remains finite, but this condition permits an infinite family of functions $\psi^{(0)}$ that satisfy the leading order Poisson equation (17), and so we require a stronger condition on ψ as $r\to\infty$ in order to determine ψ uniquely. We are therefore restricted to cases where R_I is $\mathrm{O}\,(1)$ and R_O is finite.

4 Weakly Nonlinear Waves

The evolution equation (22) descibes the fully nonlinear behaviour of our system, but it is somewhat too complicated to analyse directly. We therefore first examine the dynamics of weakly nonlinear waves by assuming that the wave amplitude is $\mathrm{O}\,(\mu)$ and that the variations in R_I, R_H and R_O are $\mathrm{O}\left(\mu^2\right)$. These scalings are chosen such that nonlinear and dispersive terms are of the same order, and such that only the leading-order effects of a radially asymmetric annulus are included. We set $R=\overline{R_H}+\mu\hat{A}$, $R_I=\overline{R_I}+\mu^2\hat{w}(\phi)$, $R_H=\overline{R_H}+\mu^2\hat{h}(\phi)$ and $R_O=\overline{R_O}+\mu^2\hat{c}(\phi)$ in (22), and retain terms up to $\mathrm{O}\left(\mu^2\right)$. Note

that the contributions from $\psi^{(2)}$ and higher-order terms will be at least $\mathrm{O}\left(\mu^3\right)$ due to the ϕ derivative on the right hand side of (22). We obtain the following weakly nonlinear wave equation,

$$\hat{A}_\tau + (\alpha+\alpha_m)\hat{A}_\phi + \mu\beta\hat{A}_{\phi\phi\phi} - \frac{\mu}{2\overline{R_H}}\left(\mathrm{sign}\left(\hat{A}\right)+\gamma\right)\hat{A}\hat{A}_\phi = -\mu\alpha\hat{h}_\phi + \mu\alpha_m\left(\delta_c\hat{c}_\phi + \delta_w\hat{w}_\phi\right), \tag{23}$$

where

$$\alpha = \frac{\ln\left(\overline{R_H}/\overline{R_I}\right)\ln\left(\overline{R_O}/\overline{R_H}\right)}{\ln\left(\overline{R_O}/\overline{R_I}\right)},\ \beta = \frac{\ln^2\left(\overline{R_H}/\overline{R_I}\right)\ln^2\left(\overline{R_O}/\overline{R_H}\right)}{3\ln\left(\overline{R_O}/\overline{R_I}\right)},\ \gamma = 3\frac{\ln\left(\overline{R_H}^2/\overline{R_O R_I}\right)}{\ln\left(\overline{R_O}/\overline{R_I}\right)},$$
$$\delta_c = \frac{\overline{R_O}\left(\overline{R_H}^2-\overline{R_I}^2\right)}{\overline{R_H}\left(\overline{R_O}^2-\overline{R_I}^2\right)},\ \delta_w = \frac{\overline{R_I}\left(\overline{R_O}^2-\overline{R_H}^2\right)}{\overline{R_H}\left(\overline{R_O}^2-\overline{R_I}^2\right)}. \tag{24}$$

The terms on the left hand side of (23) resemble those of the KdV equation, whilst those on the right are all contributions from variations of the annulus' walls and shelf line. The most significant contribution comes from variations of the shelf line $\hat{h}_\phi$, whilst variation of the walls, $\hat{c}_\phi$ and $\hat{w}_\phi$, only makes a contribution in the case that there is a mean flow ($\alpha_m \neq 0$).

For convenience, we rewrite (23) in terms of unscaled dimensionless variables by reversing the transformation (14) and setting $A = \mu\hat{A}$, $h = \mu^2\hat{h}$, $c = \mu^2\hat{c}$ and $w = \mu^2\hat{w}$. This yields the following alternative form of the weakly nonlinear wave equation,

$$A_t + (\alpha+\alpha_m)A_\theta + \beta A_{\theta\theta\theta} - \frac{1}{2\overline{R_H}}\left(\mathrm{sign}(A)+\gamma\right)AA_\theta = -\alpha h_\theta + \alpha_m\left(\delta_c c_\theta + \delta_w w_\theta\right). \tag{25}$$

The difference between (25) and KdV lies in the coefficient of the nonlinear term (AA_ϕ), which may be positive or negative depending on the sign of A and the positions of the channel walls and shelf line. It is exactly zero if

$$A>0 \text{ and } \overline{R_H} = \left(\overline{R_I}^2\overline{R_O}\right)^{1/3} = \overline{R_{H1}}, \text{ or } A<0 \text{ and } \overline{R_H} = \left(\overline{R_I R_O}^2\right)^{1/3} = \overline{R_{H2}}. \tag{26}$$

If we let $\overline{R_I}\to\infty$ then $\overline{R_{H1}}\to(2\overline{R_I}+\overline{R_O})/3$ and $\overline{R_{H2}}\to(\overline{R_I}+2\overline{R_O})/3$, which are exactly the conditions found for the analogous straight-channel case in [3]. These values of $\overline{R_H}$ define different regimes for the coefficient of the nonlinear term, and therefore for the direction in which nonlinear steepening occurs. Specifically, the direction of nonlinear steepening is always opposite to the direction of propagation, except in the cases $\overline{R_H}<\overline{R_{H1}}$ and $A>0$ or $\overline{R_H}>\overline{R_{H2}}$ and $A<0$, when the waves steepen towards the direction of propagation.

4.1 Cnoidal Waves

When A is single-signed and the annulus is radially symmetric ($R_O \equiv \overline{R_O}$, $R_H \equiv \overline{R_H}$, $R_I \equiv \overline{R_I}$), equation (25) reduces to the KdV equation, which is known [25] to possess cnoidal wave solutions. We shall restrict our attention to the case $A \leq 0$, with the understanding that the $A \geq 0$ case has analogous results. Equation (25) then becomes

$$A_t + \alpha A_\theta + \beta A_{\theta\theta\theta} + \gamma_1 AA_\theta = 0, \qquad \gamma_1 = \frac{\ln(R_O^2 R_I/R_H^3)}{R_H\ln(R_O/R_I)}. \tag{27}$$

We seek travelling wave solutions of the form $A(\theta,t)=F(\xi)$, where $\xi=\theta-(\alpha+\Delta)t$, and then apply the transformation $F(\xi)=6B(\xi)/\gamma_1$, $\xi=\sqrt{\beta}\zeta$, to obtain the standard form of the KdV equation

$$-\Delta B_\zeta+6BB_\zeta+B_{\zeta\zeta\zeta}=0. \tag{28}$$

This equation has well-documented [25] 'cnoidal' wave solutions of the form,

$$B=2p^2\kappa^2\mathrm{cn}^2(p(\zeta+\zeta_0);\kappa)+B_0, \qquad \Delta=8p^2\kappa^2-4p^2+\gamma_1 A_0, \tag{29}$$

where $0\le\kappa\le1$ is the modulus of the Jacobi elliptic cn function [1] and ζ_0, p and B_0 are constants. Thus, the cnoidal wave solutions to (27) are

$$A(\theta,t)=A_m\,\mathrm{cn}^2\left\{\frac{1}{2\kappa}\sqrt{\frac{A_m\gamma_1}{3\beta}}\,(\theta-(\alpha+\Delta)t+\theta_0)\,;\kappa\right\}+A_0, \tag{30}$$

with

$$\Delta=\gamma_1\left(A_0+\left(2-\frac{1}{\kappa^2}\right)\frac{A_m}{3}\right), \tag{31}$$

where A_0 is the reference amplitude and A_m is the maximum displacement from A_0. The argument of the cn function must be real for A to be bounded, so we must have $A_m\gamma_1\ge0$ because $\beta>0$ always. The sign of A_m is therefore determined by the position of the shelf line relative to the inner and outer walls of the annulus. Specifically, if $R_H\ge R_{H2}$ then $\gamma_1\le0$ and so $A_m\le0$. Thus $A\le0$ as long as $A_0\le0$. If $R_H\le R_{H2}$ then $\gamma_1\ge0$ and so $A_m\ge0$. Thus $A\le0$ as long as $A_0\le-A_m$.

A further restriction is imposed by the periodicity of the annular domain. The angular wave length of the cnoidal waves is

$$\lambda_\theta=4\kappa K(\kappa)\sqrt{\frac{3\beta}{A_m\gamma_1}}, \tag{32}$$

where K is the complete elliptic integral of the first kind [1]. We require that $\lambda_\theta=2\pi/n$ for any positive integer n, which yields the following expression for the wave amplitude,

$$A_m=\frac{12\beta n^2\kappa^2K^2(\kappa)}{\pi^2\gamma_1}. \tag{33}$$

Thus, for a given mode n, the amplitude of the wave A_m determines the modulus κ, and thereby the shape of the wave. Note also that because the amplitude is limited by the width of the channel, and because $\kappa K(\kappa)$ is a strictly increasing function of κ, higher-frequency modes must have smaller moduli κ, and so will be more similar to cosine waves. Meanwhile lower-frequency modes can have larger moduli and so are closer to the soliton solution ($\kappa=1$). The complete range of solutions may be written as

$$A(\theta,t)=\frac{12\beta n^2\kappa^2K^2(\kappa)}{\pi^2\gamma_1}\mathrm{cn}^2\left\{\frac{nK(\kappa)}{\pi}(\theta-(\alpha+\Delta)t+\theta_0)\,;\kappa\right\}+A_0. \tag{34}$$

Whilst these solutions describe only a small subset of the possible travelling wave solutions of (27), we may expect to see the same broad characteristics in all such solutions. That is, that the longest waves should exhibit the most nonlinear behaviour, whilst shorter waves should be well-approximated by linear theory.

4.2 Phase Plane Analysis

We will now expand our analysis of the weakly nonlinear wave equation to include travelling wave solutions that are not single-signed. Following the method used in Section 4.1, we seek travelling wave solutions of the form $A(\theta, t) = F(\xi)$, $\xi = \theta - (\alpha + \Delta)t$, which leads to the following travelling wave equation,

$$-\Delta A_\xi + \beta A_{\xi\xi\xi} - \frac{1}{2R_H}\left(\text{sign}(A) + \gamma\right) A A_\xi = 0. \tag{35}$$

Integrating with respect to ξ yields

$$-\Delta A + \beta A_{\xi\xi} - \frac{1}{4R_H}\left(\text{sign}(A) + \gamma\right) A^2 = -\Delta A_0 - \frac{1}{4R_H}\left(\text{sign}(A_0) + \gamma\right) A_0^2, \tag{36}$$

where A_0 is a reference amplitude at which $A_{\xi\xi} = 0$. Multiplying through by A_ξ allows us to integrate again to obtain

$$\tfrac{1}{2}\beta A_\xi^2 + V(A) = E, \tag{37}$$

where E is a constant and V is given by

$$V(A) = A\left[\Delta\left(A_0 - \tfrac{1}{2}A\right) + \frac{\gamma}{4R_H}\left(A_0^2 - \tfrac{1}{3}A^2\right) + \frac{1}{4R_H}\left(|A_0|A_0 - \tfrac{1}{3}|A|A\right)\right] \tag{38}$$

The critical points of (37) are defined as solutions of the equation $V'(A_c) = 0$, and their nature is determined by $V''(A_c)$: if $V''(A_c) > 0$ then the critical point is a centre, and if $V''(A_c) < 0$ then the critical point is a saddle.

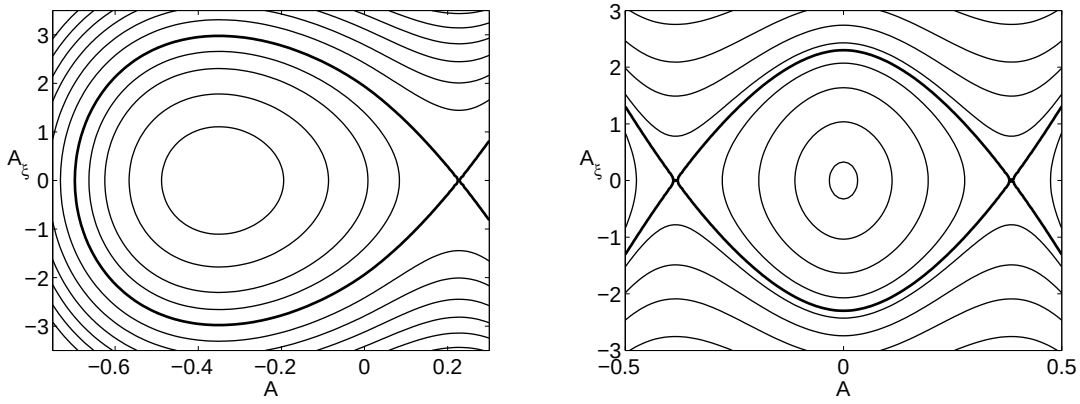

Figure 3: Phase plane for weakly nonlinear waves in the range $R_I \leq A + R_H \leq R_O$ when $R_c = 1.065\,\text{m}$, $R_h = 0.960\,\text{m}$, and (a) $R_w = 0.665\,\text{m}$, $\Delta = -0.01$, $A_0 = -0.35$, (b) $R_w = 0.8654\,\text{m}$, $\Delta = -0.02$, $A_0 = 0$. The thicker lines highlight the orbits of the critical points.

We determine the forms of the solutions by analysing the phase plane in A and A_ξ, where each contour corresponds to a different travelling wave solution. We are restricted to those

solutions whose amplitudes lie within the boundaries of the annulus, i.e. $R_I \leq R_H + A \leq R_O$. In order to fit in the annular domain, solutions must also be periodic with a period that exactly divides 2π, so only closed orbits correspond to viable solutions. The reference amplitude $A = A_0$ is always a critical point, and is always a centre as long as

$$\Delta + \frac{1}{2R_H}\left(\gamma + \operatorname{sign}(A_0)\right) A_0 < 0. \tag{39}$$

If this point is not a centre then the phase plane has no closed orbits, so this serves as a sufficient condition for there to be physical solutions.

Additionally, because we assumed in our derivation that the solution has been perturbed from a basic state in which $R = R_H$, we must ensure that mass has been in conserved in the transition to this steady solution,

$$\int_0^{2\pi} \int_{R_H}^{R} r \, \mathrm{d}r\mathrm{d}\theta = 0. \tag{40}$$

Thus, only a small subset of the curves in the phase plane are permissible as travelling wave solutions in the annulus. This excludes the possibility of the soliton solutions, which correspond to the homoclinic orbit of the critical point in Figure 3(a). In Figure 3(b) we present the case where $R_h = \sqrt{R_c R_w}$, such that $\gamma = 0$ and the nonlinear term in (35) is symmetric about $A = 0$. In this case there is a heteroclinic orbit between the saddle critical points that corresponds to the 'kink' solitons studied in [3], but again the periodicity of the domain means that such solutions are not permissible.

5 Frictional Effects

The theory of Ekman layers [22, 23, 24] suggests that the fluid in the annulus will return to solid-body rotation due to frictional effects at the base of the layer of fluid. It may be shown [18] that the leading-order effects of bottom friction can be incorporated in the rotating shallow water equations as follows,

$$\frac{\partial \mathbf{u}}{\partial t} + (\mathbf{u}\cdot\nabla)\mathbf{u} + \nabla\pi + f\hat{\mathbf{z}}\times\mathbf{u} + \frac{\tilde{k}}{\eta}\mathbf{u} = 0, \tag{41a}$$

$$\nabla\cdot(\eta\mathbf{u}) = 0, \tag{41b}$$

where $\mathbf{u} = (u, v)$ is the vertically-averaged horizontal fluid velocity, $\eta = H - h$ is the vertical thickness of the fluid layer and π is the fluid pressure at the rigid lid. The dissipation constant $\tilde{k}$ is typically inversely proportional to the Ekman spin-down time [23], $\tilde{k}/H \propto 1/\tau_E = \sqrt{f\nu/H^2} \implies \tilde{k} \propto \sqrt{f\nu}$, where τ_E is the Ekman spin-down time. The constant ν is the kinematic viscosity of the fluid in the experiment or the vertical eddy viscosity in the ocean. We will now consider the influence of friction on the system studied in Sections 3 and 4.

We first apply quasigeostrophic scaling [22, 23, 24] to (41a) and (41b). We assume that the Rossby number is very small, $\mathrm{R}o = U/fL \ll 1$, where U is a velocity scale for the flow and $L = \overline{R_c} - \overline{R_w}$ as before, and that h/H and $\tilde{k}/Hf$ are $\mathrm{O}\,(\mathrm{Ro})$. Expanding $\mathbf{u}$ and

π asymptotically in Ro then yields geostrophic balance at leading order, with contributions from friction, bottom topography and advection included at first order in a modified quasigeostrophic potential vorticity equation,

$$\frac{\mathrm{D}}{\mathrm{D}t}\left(\omega + Q\hat{h}\right) = -k\omega, \tag{42}$$

where $k = \tilde{k}/H$, and $\hat{h} = h/H_s$ is the dimensionless height of the bottom topography.

5.1 Vorticity Evolution of Fluid Columns

As in Section 3, we seek to determine the vorticity distribution and thereby formulate a nonlinear wave equation for the interface $r = R(\theta, t)$. Let us consider the vorticity $\omega_p(t)$ of an infinitesimal fluid column that lies in the region $R_w < r < R_h$ at $t = 0$, such that $\omega_p(0) = q_p(0) = 0$. Equation (42) allows us to write down an evolution equation for ω_p,

$$\frac{\mathrm{d}\omega_p}{\mathrm{d}t} + k\omega_p + Q\frac{\mathrm{d}\hat{h}_p}{\mathrm{d}t} = 0, \tag{43}$$

where $Q = fH_s/H$ as before and $\hat{h}_p(t)$ is the dimensionless height of the topography directly below the fluid column at time t. If the fluid column crosses the shelf line at times $t = t_1, t_2, \ldots, t_N$, then we may write $\hat{h}_p$ explicitly as

$$\hat{h}_p = \begin{cases} 0, & t_i < t < t_{i+1} \quad i = 0, 2, 4, \ldots, \\ 1, & t_i < t < t_{i+1} \quad i = 1, 3, 5, \ldots, \end{cases} \tag{44}$$

where we define $t_0 = 0$. Thus in $t_i < t < t_{i+1}$ for all i, $\partial\hat{h}_p/\partial t = 0$, and integrating equation (43) yields

$$\omega_p = \omega_p|_{t=t_i}\, e^{-k(t-t_i)}, \qquad t_i < t < t_{i+1}. \tag{45}$$

In order to determine the evolution of ω_p at $t = t_i$, $i = 1, \ldots, N$, we integrate (43) over $[t_i - \delta t, t_i + \delta t]$ and take the limit $\delta t \to 0$,

$$\lim_{\delta t \to 0} \int_{t_i - \delta t}^{t_i + \delta t} \left\{ \frac{\mathrm{d}\omega_p}{\mathrm{d}t} + k\omega_p + Q\frac{\mathrm{d}\hat{h}_p}{\mathrm{d}t} \right\} \mathrm{d}t = \lim_{\delta t \to 0} \left[\omega_p + Q\hat{h}_p\right]_{t_i - \delta t}^{t_i + \delta t} = 0, \tag{46}$$

where the first equality follows from the requirement that ω_p must remain finite. This condition states that potential vorticity is exactly conserved following the fluid column at the instant when it crosses the shelf line. Using (44) we may then write the jump condition for the vorticity of the fluid column as

$$[\omega_p]_{t=t_i} = (-1)^i Q, \tag{47}$$

where the square brackets [ ] denote the change of ω_p over an infinitesimally short period around $t = t_i$. Combining (45) and (47) yields the complete time-evolution of ω_p,

$$\omega_p = \begin{cases} 0, & 0 \le t < t_1, \\ Q\displaystyle\sum_{i=1}^{n} (-1)^i e^{-k(t-t_i)}, & t_n < t < t_{n+1}, \quad n < N, \\ Q\displaystyle\sum_{i=1}^{N} (-1)^i e^{-k(t-t_i)}, & t_N < t. \end{cases} \tag{48}$$

The vorticity of an infinitesimal fluid element that is initially on the shelf and that crosses the discontinuity N times may be obtained by multiplying (48) by -1.

This analysis highlights an important difference between the frictionless and frictional potential vorticity equations: in the frictionless case, fluid columns can only have non-zero vorticity if they lie between the shelf line $r = R_h$ and the interface $r = R$, whereas now every fluid column that has at any point crossed the shelf line will have nonzero vorticity. This complication means that it is no longer possible to perform a derivation similar to that described in Section 3. However, the fact that the evolution of the vorticity of individual fluid columns can be expressed in a simple form makes this system an appropriate candidate for a vortex element method [16], a Lagrangian numerical method that advects individual vortices to calculate the flow field.

5.2 Approximate Conservation Law Form

In order to include some dissipative effects in our nonlinear model, we require a conservation law that approximates (42). It is not possible to rewrite this equation in an exact conservation law form, so instead we use the following approximation,

$$\frac{\mathrm{D}}{\mathrm{D}t}\left(\omega e^{kt} + Q\hat{h}\right) = 0. \tag{49}$$

We shall now motivate this choice by considering the evolution of the total vorticity in the annulus, rather than the local vorticity field.

We obtain an evolution equation for the total vorticity by integrating (42) over the entire area of the annulus, which we denote by A,

$$\iint_A \left\{ \frac{\partial \omega}{\partial t} + k\omega + \mathbf{u} \cdot \nabla \left(\omega + Q\hat{h}\right) \right\} \mathrm{d}A = 0. \tag{50}$$

In the quasigeostrophic limit $\nabla \cdot \mathbf{u} = 0$, so we may write the final term in the integrand as

$$\iint_A \mathbf{u} \cdot \nabla \left(\omega + Q\hat{h}\right) \mathrm{d}A = \iint_A \nabla \cdot \left(\left(\omega + Q\hat{h}\right)\mathbf{u}\right) \mathrm{d}A = \int_{\partial A} \left(\omega + Q\hat{h}\right) \mathbf{u} \cdot \hat{\mathbf{n}} \, \mathrm{d}s = 0, \tag{51}$$

where ∂A denotes the horizontal boundaries of the domain, $\hat{\mathbf{n}}$ denotes a unit vector normal to the boundary, and $\mathrm{d}s$ denotes an infinitesimal unit of distance along the boundary. The second equality follows from an application of the divergence theorem, and the final equality holds because $\mathbf{u}$ must be tangential to the boundaries. Applying (51) to (50) yields the following evolution equation for the total vorticity,

$$\frac{\partial}{\partial t}\left(\langle\omega\rangle e^{kt}\right) = 0, \qquad \text{where} \qquad \langle\omega\rangle = \iint_A \omega \, \mathrm{d}A. \tag{52}$$

Via a similar procedure, it may be shown that exactly the same evolution equation for $\langle\omega\rangle$ holds in (49), which suggests that the global behaviours of (42) and (49) should be broadly similar. However, if the interface line $r = R(\theta, t)$ has been perturbed from a state where $R = R_h$ and $\omega = 0$ everywhere then this simply states that $\langle\omega\rangle = 0$ for all time, as in the frictionless case. We can therefore make a stronger evaluation of our parametrisation by considering the total absoulute vorticity in the annulus.

Recall from (48) that when $Q > 0$, the vorticity is always positive in $R_w < r < R_h$ and always negative in $R_h < r < R_c$. We shall henceforth restrict our attention to this case, with the understanding that analogous results hold when $Q < 0$. This motivates the following integration of (42),

$$\left(\iint_{A_1} - \iint_{A_2}\right)\left\{\frac{\partial\omega}{\partial t} + k\omega + \nabla\cdot\left(\left(\omega + Q\hat{h}\right)\mathbf{u}\right)\right\}\mathrm{d}A = 0 \tag{53}$$

where we have applied $\nabla\cdot\mathbf{u} = 0$ in the final term of the integrand. We define the regions $A_1 = \{(r,\theta) : R_w < r < R_h, 0 < \theta < 2\pi\}$ and $A_2 = \{(r,\theta) : R_h < r < R_c, 0 < \theta < 2\pi\}$, such that $A = A_1 \cup A_2$. Thus $\omega \geq 0$ everywhere in A_1 and $\omega \leq 0$ everywhere in A_2. The first two terms in the integrand in (53) may then be rewritten as

$$\begin{aligned}\left(\iint_{A_1} - \iint_{A_2}\right)\left\{\frac{\partial\omega}{\partial t} + k\omega\right\}\mathrm{d}A &= \left(\frac{\partial}{\partial t} + k\right)\left(\iint_{A_1} - \iint_{A_2}\right)\omega\,\mathrm{d}A \\ &= \left(\frac{\partial}{\partial t} + k\right)\left(\iint_{A_1} + \iint_{A_2}\right)|\omega|\,\mathrm{d}A = \left(\frac{\partial}{\partial t} + k\right)\langle|\omega|\rangle,\end{aligned} \tag{54}$$

where we use the shortened notation $(\iint_{A_1} - \iint_{A_2})F\,\mathrm{d}A = \iint_{A_1} F\,\mathrm{d}A - \iint_{A_2} F\,\mathrm{d}A$, and where the angular brackets $\langle\ \rangle$ denote integration over A, as in (52). The second equality in (54) follows from the fact that ω is always positive in A_1 and always negative in A_2. The final term of the integrand in (53) may be simplified using the divergence theorem,

$$\begin{aligned}I = \left(\iint_{A_1} - \iint_{A_2}\right)\nabla\cdot\left(\left(\omega + Q\hat{h}\right)\mathbf{u}\right)\mathrm{d}A &= \left(\int_{\partial A_1} - \int_{\partial A_2}\right)\left(\omega + Q\hat{h}\right)\mathbf{u}\cdot\hat{\mathbf{n}}\,\mathrm{d}s \\ &= \int_{r=R_h}\left\{\left(\omega_1 + Q\hat{h}_1\right)\mathbf{u}_1\cdot\hat{\mathbf{n}}_1 - \left(\omega_2 + Q\hat{h}_2\right)\mathbf{u}_2\cdot\hat{\mathbf{n}}_2\right\}\mathrm{d}s.\end{aligned} \tag{55}$$

Here again ∂A_1 and ∂A_2 denote the boundaries of A_1 and A_2, $\hat{\mathbf{n}}$ denotes a unit vector pointing normally outwards from the boundary, and $\mathrm{d}s$ denotes an infinitesimal distance along the boundary. The second equality in (55) follows from the requirement that $\mathbf{u}\cdot\hat{\mathbf{n}} = 0$ on $r = R_w$ and $r = R_c$, so we need only integrate over the intersection of ∂A_1 and ∂A_2, which is the shelf line $r = R_h$. The unit vectors $\hat{\mathbf{n}}_i$ are directed normally to the boundary $r = R_h$ and outwards from region A_i, so in fact $\hat{\mathbf{n}}_1 = -\hat{\mathbf{n}}_2$. Otherwise the subscripts i, where $i = 1, 2$, denote that a quantity should be evaluated infinitesimally close to the boundary in the region A_i.

Now by definition $\hat{h}_1 = 0$, and $\hat{h}_2 = 1$, and as we have taken the quasigeostrophic limit, $\mathbf{u}$ must be continuous at $r = R_h$. This allows us to further simplify our expression for I to

$$I = \int_{r=R_h}\left\{\omega_1 + \omega_2 + Q\left(\hat{h}_1 + \hat{h}_2\right)\right\}\mathbf{u}\cdot\hat{\mathbf{n}}\,\mathrm{d}s = \int_{r=R_h}\left(|\omega_1| - |\omega_2|\right)\mathbf{u}\cdot\hat{\mathbf{n}}\,\mathrm{d}s. \tag{56}$$

The second equality follows from the fact that the total mass flux across $r = R_h$ must be zero, $\int_{r=R_h}\mathbf{u}\cdot\hat{\mathbf{n}} = 0$, by conservation of mass. Thus I is the average around the shelf line of the difference between the vorticity fluxes across the shelf line. Combining (54) and (56), we obtain the following evolution equation for the total absolute vorticity in the annulus,

$$\frac{\partial}{\partial t}\left(\langle|\omega|\rangle e^{kt}\right) + Ie^{kt} = 0. \tag{57}$$

Applying the same integration to (49) yields exactly the same evolution equation for $\langle|\omega|\rangle$. The dependence of $\langle|\omega|\rangle$ on I, and thereby on the average of the vorticity field around the shelf line, means that the total absolute vorticity will evolve differently under (42) and (49).

Our parametrisation assumes, as before, that the fluid has been perturbed from a rest state with $r = R_h$ and $\omega = 0$. All vorticity then decays exponentially at a rate k, regardless of when the vorticity is generated by fluid crossing the shelf. As in the frictionless case, only fluid within the envelope of the wave (between $r = R_h$ and $r = R$) can have nonzero vorticity. Thus, this equation exactly replicates the behaviour of fluid columns that are perturbed across the shelf at $t = 0$ and remain there, or that do not cross the shelf at all. It least accurately captures the behaviour of fluid columns that cross the shelf, remain there for a period of time that is $\mathrm{O}\,(1/k)$, and then return, because these fluid columns end up outside the envelope of the wave with non-negligible vorticity. One might expect to see such behaviour, for example, in travelling wave solutions.

Nevertheless, we shall see in Section 7 that this parametrisation yields good agreement with experimental results. This is because fluid columns tend to experience a loss of vorticity when they cross the shelf line in the experiment, and so tend not to retain large vorticities outside the envelope of the waves. Equation (49) is also useful because it allows a straightforward derivation of an evolution equation for the interface $r = R$. Recalling that in the quasigeostrophic limit we have $\omega = \nabla^2\Psi$, as in Section 3, we let $\Psi_f = \Psi e^{kt}$, such that (49) becomes

$$\frac{\mathrm{D}}{\mathrm{D}t}\left(\nabla^2\Psi_f + \frac{fh}{H}\right) = 0. \tag{58}$$

We may then perform exactly the same analysis as was performed in Section 3, but replacing Ψ and ψ by Ψ_f and ψ_f throughout. The equation for the evolution of the interface is then

$$\frac{\partial R}{\partial t} = -\frac{1}{R}\frac{\partial}{\partial\theta}\Psi(R(\theta,t),\theta,t) = -\frac{e^{-kt}}{R}\frac{\partial}{\partial\theta}\Psi_f(R(\theta,t),\theta,t). \tag{59}$$

Thus, we obtain exactly the same solution for the evolution of the interface $\partial R/\partial t$, but multiplied by $\exp(-kt/Q)$, where t is now the dimensionless time. This means that the solution evolves in a way that is identical to the frictionless case, but with the motion of the interface decaying exponentially to zero.

6 Stability

The laboratory experiments with a rotating annulus have highlighed some instabilities of the fluid under certain conditions. We now examine two specific types of instability in an attempt to explain these results.

6.1 Stability of the Mean Flow

In Figure 4 we present snapshots of a laboratory experiment in which a mean flow is induced by rapidly changing the rotation rate of the annulus once the fluid is in solid body rotation. The flow becomes unstable and forms large eddies along the shelf line. It is desirable to include a mean flow in our experiments to represent the presence of a current along the shelf break, so it is of interest to determine the cause of this instability.

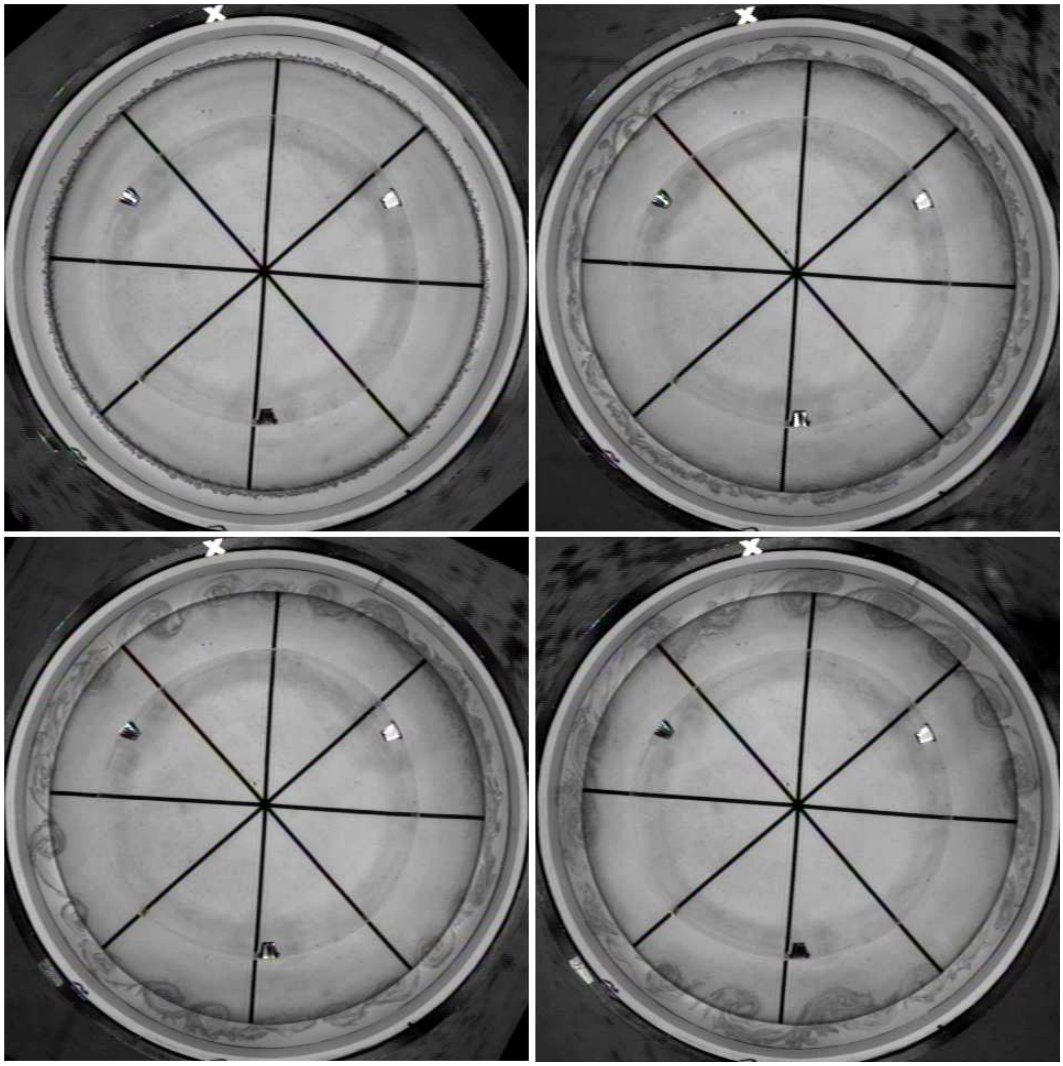

Figure 4: Snapshots of an experiment exhibiting instability to a mean flow. Once the fluid in the tank had achieved solid-body rotation, the rate of rotation of the tank was rapidly reduced from $f = 2.00\,\mathrm{rad\,s^{-1}}$ to $f = 1.85\,\mathrm{rad}\,s^{-1}$. The fluid thus continues to move anticlockwise around the tank, and develops large instabilities resembling Kelvin-Helmholz rolls as it does so. These snapshots were taken 0 (top left), 45 (top right), 59 (bottom left) and 77 (bottom right) seconds after the change in the tank's rotation rate. The maximum depth of the fluid is 25cm, and the radius of the inner wall is approximately 66cm.

Consider a mean flow $\mathbf{u}_m = v_m(r,t)\hat{\mathbf{e}}_\theta$ in a rotating annulus whose walls R_c and R_w and shelf line R_h are independent of θ, and where $\mathbf{u}_m$ is initially a flow of constant angular velocity α_0, $v_m(r,0) = \alpha_0 r$. We seek a radially symmetric solution of the dissipative shallow water equations (41a), ensuring that mass and surface pressure are conserved across the shelf line at $r = R_h$. The solution, which must be time-dependent due to the dissipative terms, is

$$v_m = \alpha_0 r e^{-\hat{k}t/\eta}, \quad \pi_m = \pi_0 + \tfrac{1}{2}\alpha_0 \left(r^2 - R_h^2\right) e^{-\hat{k}t/\eta} \left(f + \alpha_0 e^{-\hat{k}t/\eta}\right), \tag{60}$$

The fluid depth is $\eta = H - h$, where h is defined in Section 3. For $t > 0$ there is a discontinuity in v_m at $r = R_h$, and we expect that this velocity shear should be unstable to small perturbations.

To demonstrate that this configuration is unstable we consider the simple problem of a steady shear flow in the presence of a discontinuity in depth. We prescribe a mean flow of the form

$$v_m = \begin{cases} \alpha_1 r, & R_w < r < R_h, \\ \alpha_2 r, & R_h < r < R_c. \end{cases} \tag{61}$$

We might now naively seek a linear wave solution by following a method analogous to that of [17], linearising the governing equations about the mean flow solution and requiring that the mass flux and pressure across $r = R_h$ should be continuous. However, this yields a dispersion relation that has purely real modes, indicating that there is no instability in the mean flow, and that does not reduce to the expected dispersion relation when there is no discontinuity in depth. We must therefore approach the problem more carefully.

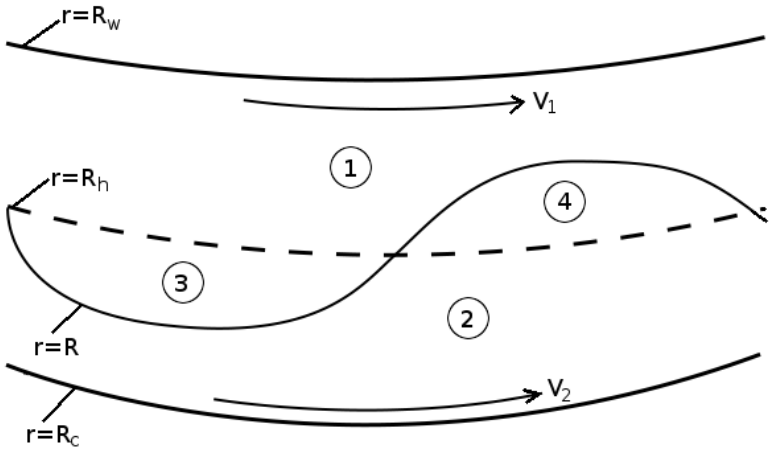

Figure 5: Schematic of a linear wave propagating in a small region of the annulus in the presence of a sheared mean flow.

Let us consider the propagation of a linear wave along the line of the shelf, presented diagrammatically in Figure 5. We split the domain into four regions, similar to the approach taken in the derivation of the nonlinear wave equation in Section 3. In order to properly

incorporate the influence of the shear, we must recognise that the mean flow in region 3 is the same as that in region 1, and similarly that the mean flow in region 4 is the same as that in region 2. The complete mean flow is then

$$\mathbf{u}_{mi} = \alpha_j r\,\hat{\mathbf{e}}_\theta, \quad \pi_{mi} = \pi_0 + \tfrac{1}{2}\alpha_j\left(r^2 - R^2\right), \tag{62}$$

where $j = 1$ for $i = 1, 3$ and $j = 2$ for $i = 2, 4$, which also ensures continuity of pressure across $r = R$ and $r = R_h$. We linearise (41a) with $\hat{k} = 0$ about the mean flow solution, setting $\mathbf{u}_i = \mathbf{u}_{m,i} + \mathbf{u}_i'$, $\pi_i = \pi_{m,i} + \pi_i'$ and $R = R_h + R'$, where $\mathbf{u}_i' \ll u_{m,i}$, $\pi_i' \ll \pi_{m,i}$ and $R' \ll L$. This yields

$$\frac{\partial \mathbf{u}_i'}{\partial t} + \alpha_j \frac{\partial \mathbf{u}_i'}{\partial \theta} + (f + \alpha_j)\hat{\mathbf{z}} \times \mathbf{u}_i' + \nabla \pi_i' = 0, \qquad \nabla \cdot \mathbf{u}_i' = 0, \tag{63}$$

which is valid everywhere except at $r = R_h$. However, in the linear limit, the fluid in regions 3 and 4 becomes infinitesimally close to the shelf line $r = R_h$, and so there we must apply the linearised form of the complete mass conservation equation (41b), rather than the two-dimensional incompressibility condition. Thus (63) holds only for $i = 1, 2$.

In order to avoid a detailed consideration of the dynamics in regions 3 and 4, we instead make use of the fact that the linearised kinematic boundary conditions and pressure continuity condition for the interface $r = R_h + R'$ are imposed on the shelf line $r = R_h$,

$$\frac{\partial R'}{\partial t} + \alpha_1 \frac{\partial R'}{\partial \theta} = u_3', \quad \frac{\partial R'}{\partial t} + \alpha_2 \frac{\partial R'}{\partial \theta} = u_2', \quad \pi_2' = \pi_3', \quad \text{on} \quad r = R_h, \quad R' > 0, \tag{64a}$$

$$\frac{\partial R'}{\partial t} + \alpha_1 \frac{\partial R'}{\partial \theta} = u_1', \quad \frac{\partial R'}{\partial t} + \alpha_2 \frac{\partial R'}{\partial \theta} = u_4', \quad \pi_1' = \pi_4', \quad \text{on} \quad r = R_h, \quad R' < 0. \tag{64b}$$

We combine these with the jump conditions for the shelf line, which state that mass flux and surface pressure must be continuous across the discontinuity in depth,

$$H u_1' = (H - H_s) u_3', \quad \pi_1' = \pi_3', \quad \text{on} \quad r = R_h, \quad R' > 0, \tag{65a}$$

$$H u_4' = (H - H_s) u_2', \quad \pi_4' = \pi_2', \quad \text{on} \quad r = R_h, \quad R' < 0. \tag{65b}$$

We may now eliminate u_3', u_4', π_3', and π_4' between (65a), (65b), (64a) and (64b). We thereby avoid any consideration of the structure of regions 3 and 4, instead connecting regions 1 and 2 directly via the following jump conditions,

$$\frac{\partial R'}{\partial t} + \alpha_1 \frac{\partial R'}{\partial \theta} = \frac{1}{\Delta_H} u_1', \quad \frac{\partial R'}{\partial t} + \alpha_2 \frac{\partial R'}{\partial \theta} = u_2', \quad \pi_1' = \pi_2', \quad \text{on} \quad r = R_h, \quad R' > 0, \tag{66a}$$

$$\frac{\partial R'}{\partial t} + \alpha_2 \frac{\partial R'}{\partial \theta} = \Delta_H u_2', \quad \frac{\partial R'}{\partial t} + \alpha_1 \frac{\partial R'}{\partial \theta} = u_1', \quad \pi_1' = \pi_2', \quad \text{on} \quad r = R_h, \quad R' < 0, \tag{66b}$$

where $\Delta_H = (H - H_s)/H \leq 1$ is the depth ratio. Note that in the absence of a mean flow, $\alpha_1 = \alpha_2 = 0$, we may reduce the boundary conditions to $(H - H_s)u_2' = H u_1'$ and $\pi_1' = \pi_2'$ at $r = R_h$ for all θ, which corresponds to the approach of [17]. In fact, this reduction can be performed for any continuous mean flow profile, and it is only in the case of a discontinuous profile that this special consideration is required.

We now make use of the fact that the velocity is divergence-free in regions 1 and 2 to write $\mathbf{u}_j' = -\nabla \times \psi_j' \, \hat{\mathbf{z}}$, and seek plane wave solutions of the form $\psi_j' = \mathrm{Re}\{\hat{\psi}_j(r) \exp[i(l\theta - \sigma t)]\}$. Taking the curl of the linearised momentum equations in (63) yields a vorticity equation that states that the vorticity must be uniformly equal to zero at all times, so $\omega_1' = \nabla^2 \psi_1' = 0$ and $\omega_2' = \nabla^2 \psi_2' = 0$. We may then solve for $\hat{\psi}_i$ subject to the boundary conditions $\psi_1' = 0$ at $r = R_w$ and $\psi_2' = 0$ at $r = R_c$. Substituting the result into (66a) and (66b) yields the following dispersion relation,

$$\sigma = \frac{1}{c_1 \Delta_H + c_2} \left\{ \tfrac{1}{2}(f_2 - \Delta_H f_1) + (\Delta_H c_1 \alpha_1 + c_2 \alpha_2)\, l \right.$$

$$\left. \pm \sqrt{\tfrac{1}{4}(f_2 - \Delta_H f_1)^2 + \Delta_H (f_2 c_1 + f_1 c_2)(\alpha_1 - \alpha_2) l - \Delta_H c_1 c_2 (\alpha_1 - \alpha_2)^2 l^2} \right\}, \qquad (67)$$

where $f_1 = f + 2\alpha_1$, $f_2 = f + 2\alpha_2$, and

$$c_1(l) = \frac{(R_h/R_w)^l + (R_h/R_w)^{-l}}{(R_h/R_w)^l - (R_h/R_w)^{-l}}, \qquad c_2(l) = \frac{(R_c/R_h)^l + (R_c/R_h)^{-l}}{(R_c/R_h)^l - (R_c/R_h)^{-l}}. \qquad (68)$$

When there is no mean flow ($\alpha_1 = \alpha_2 = 0$) this reduces to the dispersion relation for linear shelf waves in an annulus. In the case of a sheared mean flow with no topography and no rotation ($\Delta_H = 1$, $f = 0$) we recover the expected instability of all wave numbers to small perturbations.

In the short-wave limit, $c_1, c_2 \to \pm 1$ as $l \to \pm\infty$, so the term proportional to l^2 in the square root of (67) causes σ to have a positive complex component proportional to l for sufficiently large l. Thus very short waves are always unstable. However, for small l the frequency may become real, and so long waves may be stable. It may be shown that in the limit of infinitely long waves, $l \to 0$, σ is real if the velocity shear, $\alpha_1 - \alpha_2$, satisfies

$$\left| \frac{\alpha_1 - \alpha_2}{\frac{1}{2}(f_1 \ln(R_h/R_w) + f_2 \ln(R_c/R_h))} - 1 \right| < \sqrt{1 + \frac{(f_2 - \Delta_H f_1)^2 \ln(R_c/R_h) \ln(R_h/R_w)}{\Delta_H (f_1 \ln(R_h/R_w) + f_2 \ln(R_c/R_h))^2}}. \qquad (69)$$

This is not an exact condition for the velocity shear because α_1 and α_2 appear within f_1 and f_2. However, typically in both the laboratory experiments and in the ocean, $\alpha_1, \alpha_2 \ll f$, and so (69) still provides us with some insight. Long waves are stable as long as the shear is sufficiently small. For $f > 0$ a comparatively small negative shear ($\alpha_1 < \alpha_2$) will make all wave numbers unstable, whereas a relatively large positive shear ($\alpha_1 > \alpha_2$) is required to achieve the same effect. In Figure 6 we present plots of the real and imaginary parts of (67) for typical experimental parameter values with a positive shear.

Long waves can be stabilised because the generation of vorticity within the envelope of the wave creates a velocity shear about the shelf line. This shear, which is most pronounced in long waves, may exceed the size of the mean shear and thereby stabilise the disturbances. Despite this, short waves are almost completely unaffected by the presence of rotation and a discontinuity in depth. Although we still expect the shortest waves to be the most unstable, the largest instabilities in the experiment of Figure 4 have wavelengths on the order of 30cm, so in fact the longer perturbations grow faster in practice. Thus, whilst our idealised theory can qualitatively predict this instability, we require a more sophisticated treatment to make realistic quantitative predictions.

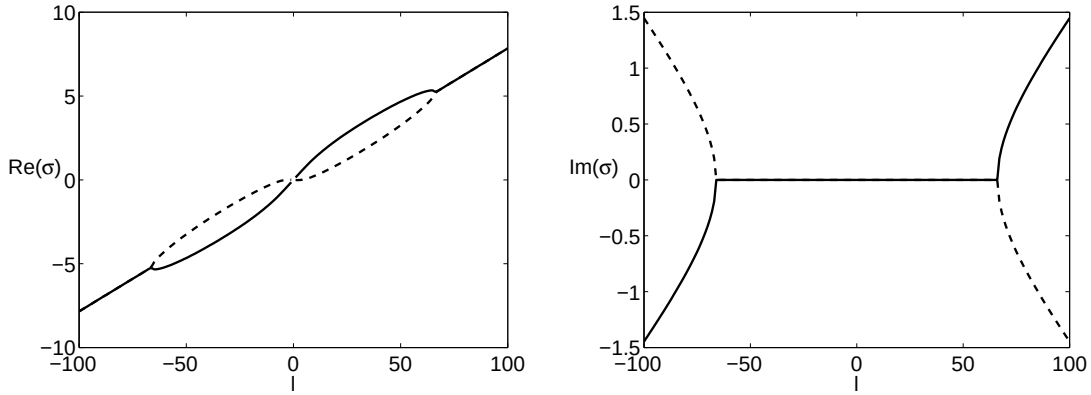

Figure 6: Real (left) and imaginary (right) parts of the dispersion relation for linear waves propagating in the presence of a sheared mean flow. Here $f = 1.5\,\mathrm{rad\,s^{-1}}$, $\alpha_1 = 0.1\,\mathrm{rad\,s^{-1}}$, $U_2 = 0.05\,\mathrm{rad\,s^{-1}}$, $\Delta_H = 0.8$, $R_w = 66\,\mathrm{cm}$, $R_h = 96\,\mathrm{cm}$ and $R_c = 106.5\,\mathrm{cm}$, as in the experiment shown in Figure 4.

6.2 Stability of Long Waves

We now turn our attention to another laboratory experiment, illustrated in Figure 7. Here a long wave is generated by reducing the rotation rate of the tank for a few seconds, creating a temporary mean flow that generates a perturbation past a long bump in the outer wall. The perturbation quickly breaks up into short waves, with the rest of the dyed interface following suit shortly afterwards. This raises the possibility that the nonlinear topographic Rossby waves themselves may be intrinsically unstable.

We perform a simple stability analysis of the waves by using the fact that they are long and slowly-varying to approximate them as a radially symmetric strip of constant vorticity ω_0, as shown in Figure 8. We retain the shelf line at $r = R_h$, but for now we let ω_0 be arbitrary, and do not require it to be equal to Q as we did in Section 3. We shall also only consider the case where $R > R_h$, as in the experiment shown in Figure 7, with the understanding that similar results hold in the case that $R < R_h$. In the analogous problem for a straight channel with a symmetric strip of constant vorticity [5], the flow is found to be unstable to long waves if the width of the strip is less than half the width of the channel.

We write the basic-state vorticity as

$$\overline{\omega} = \omega_0 \left[\mathcal{H}(r - R) - \mathcal{H}(r - R_h)\right], \tag{70}$$

as in (10), where the bar notation $\overline{\ }$ will be used henceforth to denote the basic flow. This means that for $\omega_0 > 0$, $\overline{\omega} < 0$ in $R_h < r < R$, reflecting the $f > 0$ case in Section 3. We seek a radially symmetric basic flow $\overline{\mathbf{u}} = \overline{v}(r)\hat{\mathbf{e}}_\theta$, which by definition is incompressible, $\nabla \cdot \overline{\mathbf{u}} = 0$. The corresponding streamfunction $\overline{\psi}$ matches the leading-order streamfunction (18) from Section 3 exactly, subject to the requirement that it must be uniformly equal to zero on the

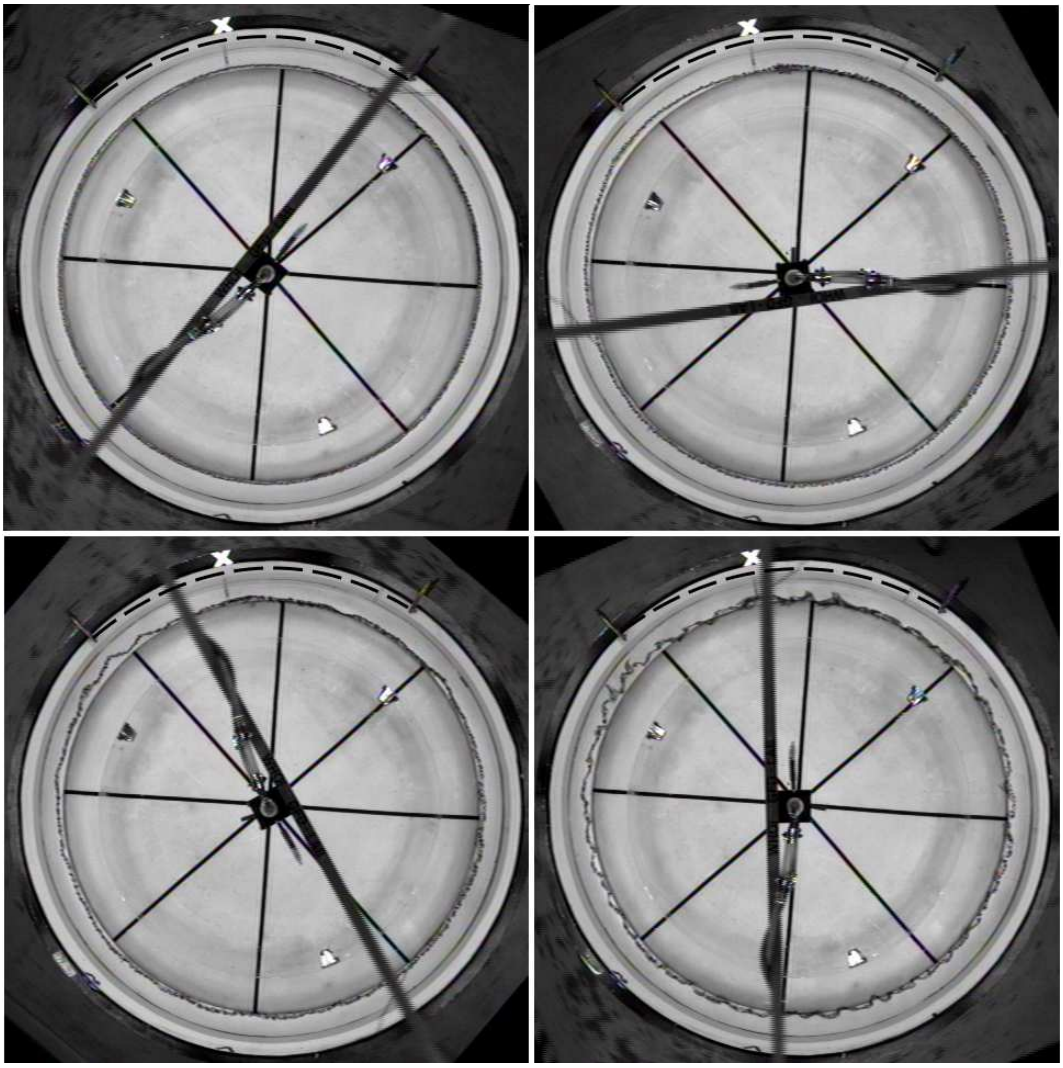

Figure 7: Snapshots of an experiment in which an instability arises in a long perturbation. Once the fluid in the tank had achieved solid-body rotation (top left), the rate of rotation of the tank was rapidly decelerated from $f = 1.50\,\mathrm{rad\,s^{-1}}$ to $f = 1.20\,\mathrm{rad\,s^{-1}}$, and then rapidly accelerated again to $f = 1.45\,\mathrm{rad\,s^{-1}}$. The effect of this is to cause the fluid to move anticlockwise around the tank for 6 seconds and then return to approximate solid-body rotation. A bump in the side wall of length 1.5m and maximum amplitude 2cm, highlighted in the diagram by the superposed dashed lines, leads to the formation of a perturbation ahead of the bump (top right). After 12 seconds (bottom left), a growing short wave instability appears in the perturbation, and after 17 seconds this instability is affecting the entire annulus. The maximum depth of the fluid in this experiment is 20cm, and the radius of the inner wall is approximately 75cm.

walls $r = R_w$ and $r = R_c$. Thus the basic-state velocity is

$$\overline{v}(r) = \frac{\omega_0}{2r}\left[\mathcal{H}(r-R)(r^2-R^2) - \mathcal{H}(r-R_h)(r^2-R_h^2) + \frac{\frac{1}{2}(R^2-R_h^2) + R^2\ln(R_c/R) - R_h\ln(R_c/R_h)}{\ln(R_c/R_w)}\right]. \tag{71}$$

Note that although the vorticity is discontinuous at $r = R$ and $r = R_h$, the velocity is continuous at both radii. The corresponding basic-state surface pressure satisfies $\mathrm{d}\overline{\pi}/\mathrm{d}r = f\overline{v} + \overline{v}^2/r$, but its exact form has no bearing on the stability of the flow.

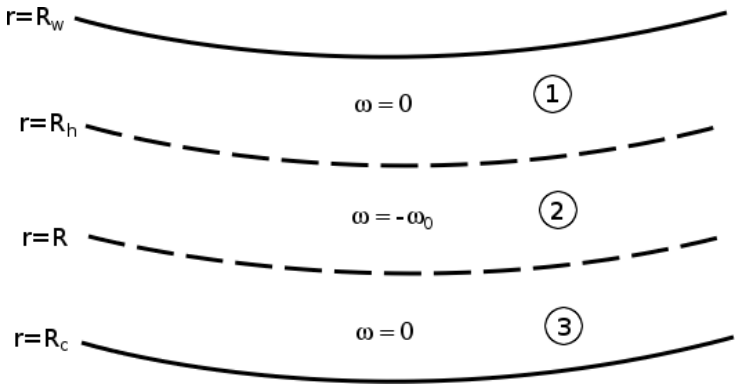

Figure 8: A strip of constant vorticity in a section of the annulus, approximating a long, slowly-varying topographic Rossby shelf wave.

We now consider infinitesimal perturbations to the basic state, setting $\mathbf{u} = \overline{\mathbf{u}} + \mathbf{u}'$ and $\pi = \overline{\pi} + \pi'$, where $\mathbf{u}' \ll \overline{\mathbf{u}}$ and $\pi' \ll \overline{\pi}$. Substituting these into the non-dissipative shallow water equations, (41a) and (41b), and linearising yields

$$\frac{\partial u_j'}{\partial t} + \frac{\overline{v}}{r}\frac{\partial u_j'}{\partial \theta} - \left(f + \frac{2\overline{v}}{r}\right)v_j' + \frac{\partial \pi_j'}{\partial r} = 0, \tag{72a}$$

$$\frac{\partial v_j'}{\partial t} + \frac{\overline{v}}{r}\frac{\partial v_j'}{\partial \theta} + \left(f + \frac{\overline{v}}{r} + \frac{\partial \overline{v}}{\partial r}\right)u_j' + \frac{1}{r}\frac{\partial \pi_j'}{\partial \theta} = 0, \tag{72b}$$

$$\nabla \cdot \mathbf{u}_j' = 0, \tag{72c}$$

for $j = 1, 2, 3$, which is valid everywhere except at $r = R_h$. We connect regions 1 and 2 across $r = R_h$ and regions 2 and 3 across $r = R$ by requiring that an interface propagating about either of them should satisfy kinematic boundary conditions and continuity of surface pressure. At $r = R$, these reduce to

$$u_2' = u_3', \qquad \pi_2' = \pi_3', \qquad \text{at} \quad r = R. \tag{73}$$

At $r = R_h$ we must also ensure that mass flux and surface pressure are continuous across the discontinuity in depth. An analysis similar to that performed in Section 6.1 shows that,

because the basic velocity $\overline{v}$ is continuous, these are exactly the jump conditions required to connect regions 1 and 2,

$$Hu_1' = (H - H_s)u_2', \qquad \pi_1' = \pi_2', \qquad \text{at} \quad r = R_h. \tag{74}$$

Taking the curl of (72a) and (72b) yields the vorticity equation

$$\frac{\partial \omega_j'}{\partial t} + \frac{\overline{v}}{r}\frac{\partial \omega_j'}{\partial \theta} + u_j'\frac{\partial \overline{\omega}}{\partial r} = 0. \tag{75}$$

The last term on the left hand side of this equation is equal to zero because $\overline{\omega}$ is piecewise-constant. Thus, if we seek plane wave solutions of the form $\psi_j' = \mathrm{Re}\{\hat{\psi}_j \exp[i(l\theta - \sigma t)]\}$, then (75) states that $\omega_j' = 0$ holds everywhere except at $r = R_h$.

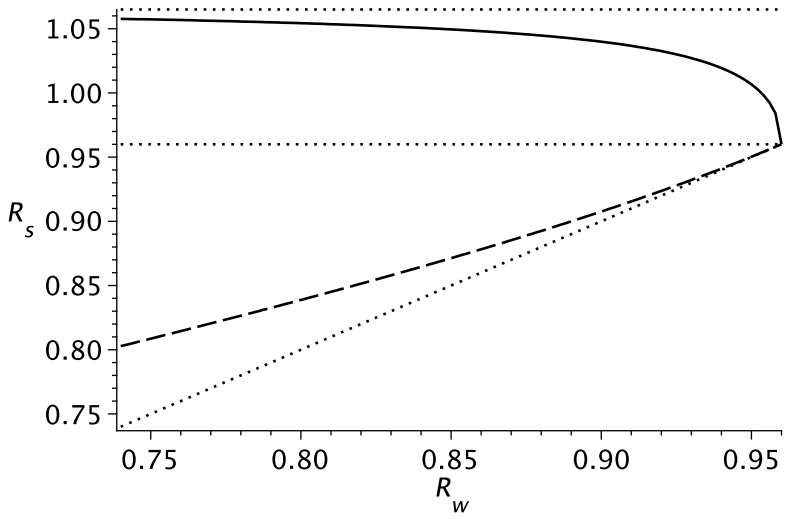

Figure 9: Plot of the stability radius R_s (in metres) for the case $R > R_h$ (solid line), defined such that if $R_h < R < R_s$ then the flow is unstable, but for $R_s < R < R_c$ the flow is stable. We also show the stability radius for the case $R < R_h$ (dashed line), defined such that if $R_s < R < R_h$ then the flow is unstable, but for $R_w < R < R_s$ the flow is stable. The dotted lines mark the positions of the outer wall R_c, the shelf line R_h and the inner wall R_w.

We may now obtain the complete solution using $\omega_j = \nabla^2 \psi_j' = 0$ in region j for $j = 1, 2, 3$, which has the solution

$$\psi_j' = \mathrm{Re}\left\{\left(A_j r^l + B_j r^{-l}\right) e^{i(l\theta - \sigma t)}\right\}, \tag{76}$$

where A_j and B_j are constants. We then apply the jump conditions (73) and (74), and the boundary conditions $\psi_1' = 0$ on $r = R_w$, $\psi_3' = 0$ on $r = R_c$. This determines all of the constants A_j, B_j in terms a single constant representing the amplitude of the wave, which remains arbitrary, and yields a dispersion relation for the wave frequency $\sigma(l)$. Unfortunately the calculation quickly becomes too complicated to obtain meaningful analytical results, and is best handled using symbolic computation packages and numerical calculation. We find that if there is no shelf ($\Delta_H = 1$) then, as in the case of a straight channel, the flow

is unstable to long waves ($l \to 0$) unless one of the discontinuities lies sufficiently close to the edge of the channel. The stability here is also independent of the vorticity ω_0 and the Coriolis parameter f. This is illustrated in Figure 9.

If we include a shelf ($\Delta_H < 1$) then, as we found in Section 6.1, long waves may be stabilised. In Figure 10 we compare $\sigma(l)$ between cases where $\Delta_H = 0.75$ and $\Delta_H = 1$, with all other parameters chosen to match the experiment presented in Figure 7. We see that the flow is stable to all wave numbers in the presence of the shelf, but is unstable to long waves when the shelf is absent. The most unstable wave in the latter case has a length of approximately $\pi/16$ radians, which almost exactly matches the the length of the instabilities observed in the bottom-left frame in Figure 7. This raises the possibility that the stability of the long nonlinear wave in this experiment, which utilised an absolute discontinuity in the bottom topography, is not affected by the shelf.

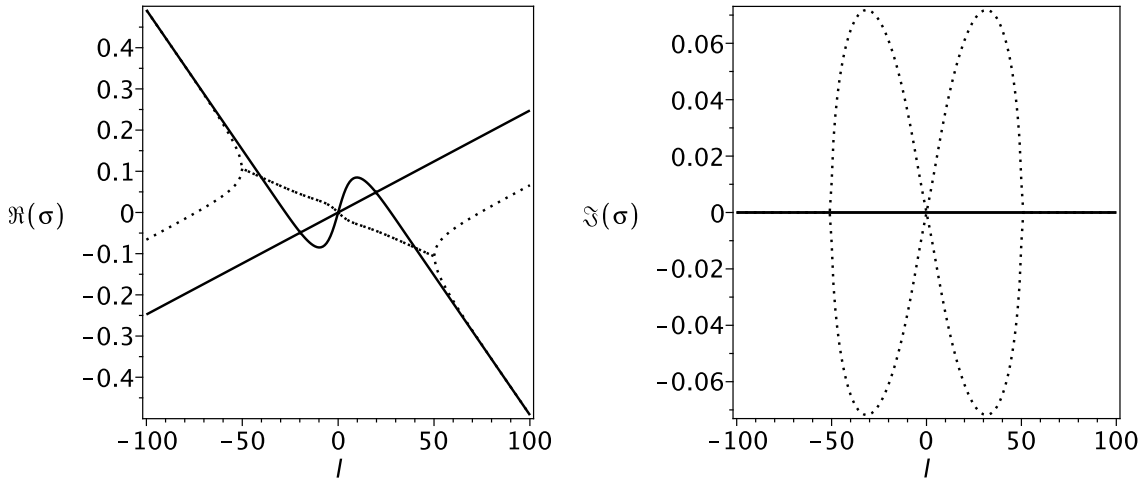

Figure 10: Plot of the wave frequency σ in rad s^{-1} as a function of the wave number l in rad^{-1} for linear perturbations to an annular strip of vorticity, where $R_w = 0.75\,\mathrm{m}$, $R_h = 0.96\,\mathrm{m}$, $R = 0.985\,\mathrm{m}$ and $R_c = 1.065\,\mathrm{m}$. The solid line corresponds to the wave frequency when there is a discontinuity in depth ($\Delta_H = 0.75$) at $r = R_h$, whilst the dotted line corresponds to the case of no discontinuity in depth ($\Delta_H = 1$). In both cases $f = 1.45\,\mathrm{rad\,s^{-1}}$ and $\omega_0 = 0.3625\,\mathrm{rad\,s^{-1}}$, corresponding the theoretical vorticity of the nonlinear topographic Rossby wave in Figure 7.

The analysis performed here is based on infinitesimal horizontal perturbations to the fluid directly above the discontinuity. To comply with this theory, fluid columns are required to cross the discontinuity rapidly and repeatedly, which is physically counter-intuitive, so it is not surprising to see that this analysis breaks down. If indeed the stability of long topographic Rossby shelf waves propagating about an absolute discontinuity in depth is determined by the theory for the case of a flat channel, then we should expect almost all such waves to be unstable, according to Figure 9. However, in both the real ocean and in the later laboratory experiments, the discontinuity in the theory is actually an approximation of a slope, whose width is assumed to be negligible compared to the amplitude of the

waves. This casts doubt upon the validity of the linear theory, which assumes waves of infinitesimally small amplitude. In order to accurately examine the stability of these waves, we would require a considerably more complex treatment of the problem that accounted for the slope connecting the regions of different depths across the shelf line.

7 Breaking Lee Waves

We shall now turn our attention to waves generated in the lee of a bump in the outer wall of the annulus. Of all of the experiments performed in the course of this project, these were the only ones that led to consistent and measurable results, as most were subject to rapidly growing instabilities similar to those described in Section 6.

In Figure 11 we present a specimen experiment in which a bump has been created on the inside edge of the tank using the deformable wall. This is compared with a numerical solution to the nonlinear wave equation (22), computed using a pseudo-spectral code. Once the fluid had reached solid-body rotation, we rapidly increased the rate of rotation of the tank from $f = 1.50\,\mathrm{rad\,s^{-1}}$ to $f = 1.60\,\mathrm{rad\,s^{-1}}$ for 6 seconds, and then returned the rotation rate to $f = 1.54\,\mathrm{rad\,s^{-1}}$. This resulted in the generation of a wave behind the bump and a mean flow of $\alpha_m \approx -0.02\,\mathrm{rad\,s^{-1}}$. This state is used as the starting point ($t = 0\,\mathrm{s}$) of the experiment for the purpose of numerical calculation, and corresponds to the top frame in each of the series of images in Figure 11.

In the laboratory experiment, both with and without a sloping shelf, the long lee wave breaks at the end furthest from the shelf after approximately 8 seconds. This is not possible in the numerical solution of the full nonlinear wave equation (22), as dispersion will always "smooth out" any large gradients. We therefore also present the numerical solution when the dispersive $\mathrm{O}(\mu)$ terms are excluded, visible only in the second frame of the numerical solution. In Figure 12 we compare the length of the lee wave at the point of breaking between the experiments and the non-dispersive computations for a range of mean flow speeds. We also plot the dispersive wavelengths at times correspoinding to the point of wave breaking in the experiments. These results suggest that the dispersive theory accurately predicts the wavelength for mean flow speeds less than -0.01 rad $\mathrm{s^{-1}}$, whilst the non-dispersive theory is more accurate for larger mean flow speeds. However, there is some uncertainty in the wavelength and exact time of breaking in the experiment. For $\alpha_m > 0.01\,\mathrm{rad\,s^{-1}}$ the wave is drawn under the bump in the wall before breaking can occur, whilst for $\alpha_m < -0.02\,\mathrm{rad\,s^{-1}}$ the wave tends to be swept away from the bump by the strong mean flow.

At later times the behaviour of the experiments and the numerical solution diverge from one another. In the presence of a steep slope, the wave grows in length and amplitude, building up behind the bump in the wall. Meanwhile, instabilities arise at the end of the wave furthest from the bump, and subsequently grow into short breaking waves. Thus the wave gradually sheds vorticity and its amplitude slowly decays. By contrast, in the presence of a discontinuous shelf the wave quickly loses energy and decays back down to the shelf line. In the numerical solution, the wave also build up behind the bump in the wall, but remains there because it can not shed vorticity. The dissipation introduced via the parameterisation of section 5 gradually slows all motion of the interface, such that the wave eventually comes to rest behind the bump. The behaviour described here was found to be similar for any negative mean flow, $\alpha_m < 0$. For $\alpha_m \geq 0$ the wave moves under the

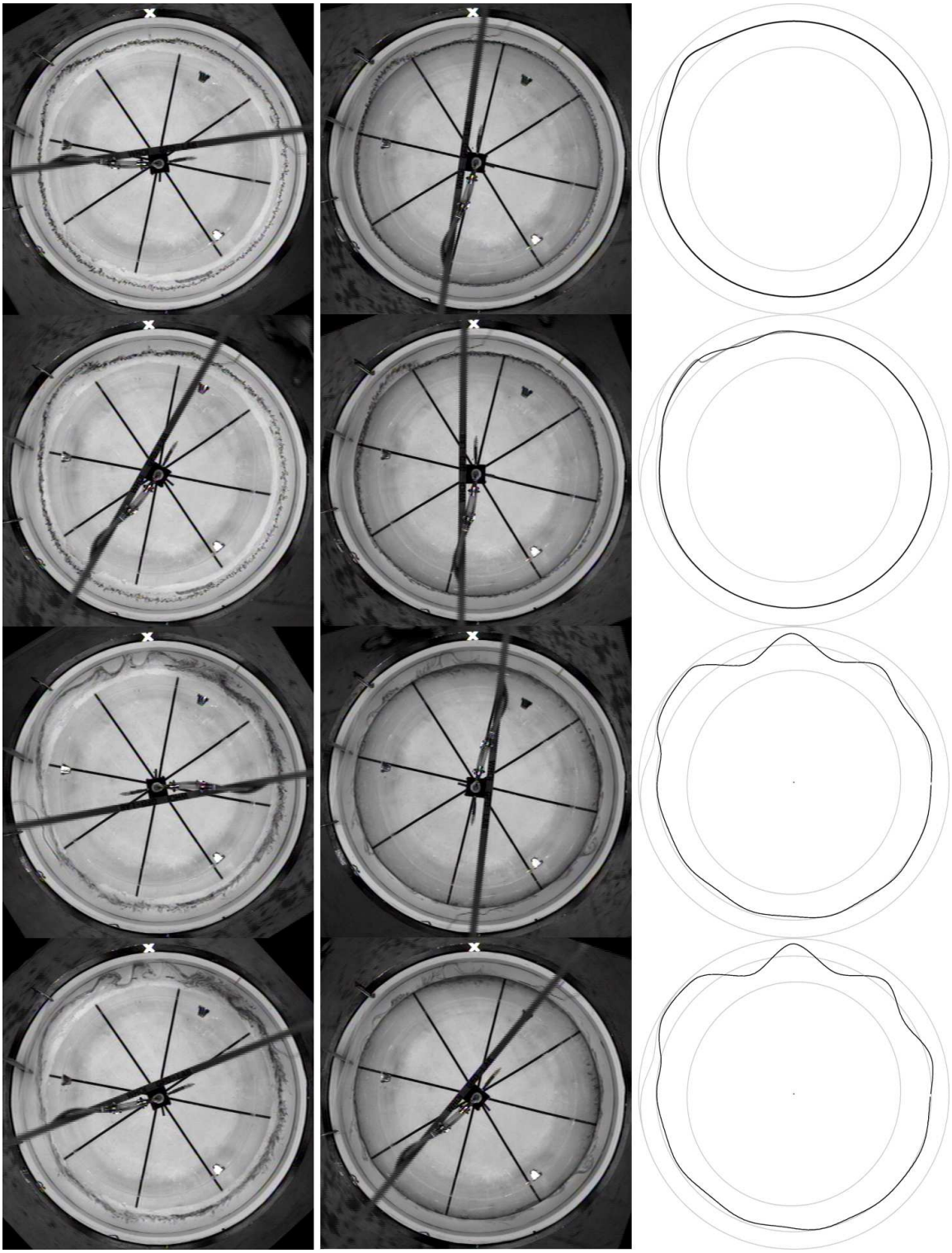

Figure 11: Snapshots of an experiment with a sloping shelf (left), and a discontinuous shelf (middle), and in a numerical solution (right) of the nonlinear wave equation with (black line) and without (dark grey line) its dispersive terms. The pictures have been taken 0, 8, 94 and 113 seconds after the generation of the lee wave.

bump, but friction around the shelf line causes it to decay rapidly as it does so.

As was mentioned in Section 2, the most serious deviation of the experiment from the theory was the use of an actual discontinuity in the depth. This experiment suggests that the fluid loses substantially more energy in crossing the discontinuous shelf than it does in crossing the steeply sloping shelf. Intuitively, this is because a Stewartson boundary layer will form at vertical wall of the shelf, whereas the sloping shelf will only have a bottom Ekman layer (see [22], p219). We therefore expect fluid columns to encounter more resistance as they cross the discontinuity than they do when they cross the slope.

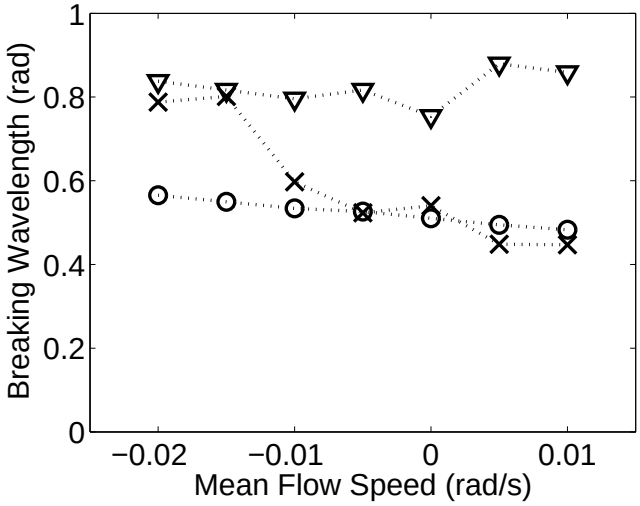

Figure 12: A comparison of the lengths of breaking lee waves in laboratory experiments (crosses) and nondispersive computations (circles), defined as the angular distance from the point of breaking to the front of the wave. In the dispersive computations (triangles), the length of the region of positive amplitude is calculated at the time of breaking in the corresponding laboratory experiment.

Between the dispersive and non-dispersive nonlinear wave equations, the main features of the flow in the sloping shelf experiment are captured quite well. The instability that arises in the lee waves may be due to a mechanism similar to that discussed in Section 6.2, but there is no reason to expect that linear analysis to apply to the case of a sloping shelf. Either way, it seems that short-wave processes invariably become important within a finite time.

8 Conclusion

This project was initially conceived as a means of testing the fundamental theory of nonlinear long Rossby shelf waves in a channel, but it has broadened to cover a much wider range of topics. The traditional theory for a straight channel has been redeveloped for application to an annular domain, and extended to include the effects of irregular walls, yielding a similar nonlinear wave equation (22). In the weakly nonlinear limit, the equation

is exactly the same as that found in the straight-channel case, but with slightly different coefficients, so the amplitude of weakly nonlinear waves is too small for them to be affected by the geometry of the annulus. The additional requirements that the waves must fit into the annular domain, and conserve mass about the shelf line, severely constrain the types of solution that are possible, and suggest that longer waves should exhibit the most nonlinear behaviour.

We have also considered the way that bottom friction might act to dissipate energy from the system. Even a simple representation of this dissipation in the quasigeostrophic shallow water equations is impossible to include exactly in our nonlinear wave model, so we constructed an alternative parametrisation on the basis of conservation laws for the global vorticity.

In the experiment itself, the waves generated were found to deviate from the long-wave theory in two important ways: they were able to break, and they were unstable to shorter waves. We explored possible mechanisms for the observed instabilities in Section 6, where a linear analysis showed that a mean flow about a discontinuity should be unstable, and that long waves of sufficiently small amplitude should themselves be unstable to long perturbations. A comparison with the experiment depicted in Figure 7 suggests that in fact the stability may be unaffected by the presence of the shelf line, explaining the observed instability at somewhat larger amplitudes.

The experiments discussed in Section 7 exhibited both breaking of long waves and instability to shorter waves that themselves subsequently went on to break. The fact that the instability arises at the rear of the lee waves, where the amplitude approaches zero, suggests an agreement with the linear stability theory. Meanwhile, the breaking of long waves suggests that in reality, dispersive effects are not strong enough to counteract the nonlinear steepening of the waves. Thus, although the nonlinear long-wave theory provides a good qualitative description of the behaviour, in practice short-wave phenomena tend to become just as important in a short time.

Acknowledgements

I would like to thank Ted Johnson, with whom I developed the ideas for the laboratory experiment and this project, for his supervision over the summer. I would also like to thank Karl Helfrich and Harvey Segur for useful meetings and discussions throughout the project. I am particularly grateful to Anders Jensen for putting much time and effort into helping me with the construction of this experiment. Finally, thanks to all of the fellows and staff for an inspiring and highly enjoyable summer at Woods Hole.

References

[1] M. Abramowitz and I. A. Stegun, *Handbook of Mathematical Functions with Formulas, Graphs, and Mathematical Tables*, Dover, New York, ninth Dover printing, tenth GPO printing ed., 1964.

[2] H. Bryden, L. Beal, and L. Duncan, *Structure and transport of the Agulhas Current and its temporal variability*, Journal of Oceanography, 61 (2005), pp. 479–492.

[3] S. Clarke and E. Johnson, *Finite-amplitude topographic Rossby waves in a channel*, Physics of Fluids, 11 (1999), pp. 107–120.

[4] ——, *The weakly nonlinear limit of forced Rossby waves in a stepped channel*, Proceedings: Mathematics, Physical and Engineering Sciences, (2001), pp. 2361–2378.

[5] P. Drazin and W. Reid, *Hydrodynamic Stability*, Cambridge University Press, Cambridge, 1981.

[6] A. Gill and E. Schumann, *Topographically induced changes in the structure of an inertial coastal jet: Application to the Agulhas Current*, Journal of Physical Oceanography, 9 (1979), pp. 975–991.

[7] P. Haynes, E. Johnson, and R. Hurst, *A simple model of Rossby-wave hydraulic behaviour*, Journal of Fluid Mechanics, 253 (1993), pp. 359–384.

[8] A. Hinds, I. Eames, E. Johnson, and N. McDonald, *Laboratory study of vortex dipoles interacting with step topography*, Journal of Geophysical Research-Oceans, 114 (2009), pp. C06006–+.

[9] A. Hinds, E. Johnson, and N. McDonald, *Vortex scattering by step topography*, Journal of Fluid Mechanics, 571 (2007), pp. 495–505.

[10] E. Johnson, *Topographic waves and the evolution of coastal currents*, Journal of Fluid Mechanics, 160 (1985), pp. 499–509.

[11] E. Johnson and S. Clarke, *Dispersive effects in Rossby-wave hydraulics*, Journal of Fluid Mechanics, 401 (1999), pp. 27–54.

[12] ——, *Rossby Wave Hydraulics*, Annual Review of Fluid Mechanics, 33 (2001), pp. 207–230.

[13] E. Johnson and M. Davey, *Free-surface adjustment and topographic waves in coastal currents*, Journal of Fluid Mechanics, 219 (1990), pp. 273–289.

[14] E. Johnson, A. Hinds, and N. McDonald, *Steadily translating vortices near step topography*, Physics of Fluids, 17 (2005), pp. 056601–+.

[15] E. Johnson and N. McDonald, *Surf-zone vortices over stepped topography*, Journal of Fluid Mechanics, 511 (2004), pp. 265–283.

[16] A. Leonard, *Vortex methods for flow simulation*, Journal of Computational Physics, 37 (1980), pp. 289–335.

[17] M. Longuet-Higgins, *On the trapping of waves along a discontinuity of depth in a rotating ocean*, Journal of Fluid Mechanics, 31 (1968), pp. 417–434.

[18] F. Marche, *Derivation of a new two-dimensional viscous shallow water model with varying topography, bottom friction and capillary effects*, European Journal of Mechanics/B Fluids, 26 (2007), pp. 49–63.

[19] L. Mysak, *Recent advances in shelf wave dynamics*, Reviews of Geophysics, 18 (1980), pp. 211–241.

[20] ——, *Topographically trapped waves*, Annual Review of Fluid Mechanics, 12 (1980), pp. 45–76.

[21] L. Mysak, P. Leblond, and W. Emery, *Trench waves*, Journal of Physical Oceanography, 9 (1979), pp. 1001–1013.

[22] J. Pedlosky, *Geophysical Fluid Dynamics*, Springer, 1987.

[23] R. Salmon, *Lectures on geophysical fluid dynamics*, Oxford University Press, USA, 1998.

[24] G. Vallis, *Atmospheric and oceanic fluid dynamics: fundamentals and large-scale circulation*, Cambridge University Press, 2006.

[25] G. Whitham, *Linear and nonlinear waves*, Wiley-Interscience, 1974.